Journal of The Electrochemical Society, 2024 **171** 080537

Enhanced Porous Electrode Theory Based Electrochemical Model for Higher Fidelity Modelling and Deciphering of the EIS Spectra

Igor Mele,[1] Klemen Zelič,[1] Marko Firm,[2] Jože Moškon,[2] Miran Gaberšček,[2,3] and Tomaž Katrašnik[1,z]

[1]*University of Ljubljana, Faculty of Mechanical Engineering, SI-1000 Ljubljana, Slovenia*
[2]*National institute of Chemistry, Department of Materials Chemistry, SI-1000 Ljubljana, Slovenia*
[3]*University of Ljubljana, Faculty of Chemistry and Chemical Technology, SI-1000 Ljubljana, Slovenia*

Electrochemical impedance spectroscopy (EIS) is essential for non-invasive battery characterization. This paper addresses the challenge of adequate interpretation of EIS spectra, which are often complicated by overlapping internal phenomena occurring on similar time scales. We present, for the first time, a high-fidelity numerical time-domain electrochemical model that can virtually replicate experimental EIS spectra with three superimposed high-frequency semicircles, a transition to the diffusion tail at elevated imaginary values, and a tilted diffusion tail at low frequencies. These advanced features were made possible by extending state-of-the-art porous electrode model with innovative sub-models for the double layer phenomenon at the carbon black/electrolyte and metal Li-anode/electrolyte interfaces, and transport phenomena of charged species through the solid electrolyte interphase at the Li-anode interface. Additionally, we modelled the diffusion tail inclination by introducing representative active particles of varying sizes. Results from custom-made half-cells confirm the model's ability to decipher EIS spectra more accurately compared to existing models. Moreover, innovative physics-based battery model that is capable of accurately modelling intra-cell phenomena can reveal internal states and physical parameters of batteries using measured EIS spectra. The model, therefore, also enables functionality of an advanced virtual sensor, which is an important diagnostics feature in next-generation battery management systems.

 [DOI: 10.1149/1945-7111/ad6eb9]

Manuscript submitted May 30, 2024; revised manuscript received August 4, 2024. Published August 27, 2024.

Supplementary material for this article is available online

Greek letters

α	Charge transfer coefficient [−]
ϵ	Porosity [−]
κ	Liquid phase conductivity [S/m]
μ	Chemical potential [J/mol]
Φ	Potential [V]
ϕ	Ratio [−]
ρ	Density [kg/m^3]
σ	Solid phase conductivity [S/m]

Latin letters

$\bar{c}$	Average concentration [mol/m^3]
a	Specific surface [1/m]
C	Capacitance [F/m^2]
c	Concentration [mol/m^3]
D	Diffusion constant [m^2/s]
E	Cell voltage [V]
F	Faraday constant [As/mol]
f	Activity coefficient [−]
I	Current density [A/m^2]
i	Current density [mol/m^{2}s]
j	Reaction rate per unit area [mol/m^{2}s]
L	Length [m]
M	Molar mass [kg/mol]
m	Mass [kg]
R	Gas constant [J/mol K]
r	Coordinate in particle's radial direction [m]
S	Electrode surface [m^2]
T	Temperature [K]
t	Transference number [−]
V	Volume [m^3]
x	Coordinate across the cell length [m]
z	Charge of the species [−]
Q	Capacity [Ah]
x	Lithiation level [mol]
Z	Impedance [Ω]

Subscripts or superscripts

±	Positively or negatively charged species
+	Positively charged species
a	Anodic
am	Active material
app	Applied
b+cb	Binder and carbon black
brugg	Bruggeman
BV	Butler-Volmer
c	Cathodic
cat	Cathode
DL	Double layer
e	Electrolyte
ecb	Electrolyte/carbon black interface
eLi	Electrolyte/Li-anode interface
es	Electrolyte/solid interface
GITT	Galvanostatic intermittent titration technique
Li	Lithium
p	Particle
ref	Reference
s	Solid
sep	Separator
th	Theoretical
V	Volume

Modelling plays a crucial role in the development process of advanced Li-ion batteries. On the one hand, it is crucial for a better understanding of the fundamental physico-chemical processes. On the other hand, if models have a sufficiently high consistency with the real underlying phenomena taking place in batteries and thus a sufficiently high predictive capability, they are an important building block for the virtualisation of the development process and enable efficient exploration of the design space and virtual prototyping. Battery materials, such

[z]E-mail: tomaz.katrasnik@fs.uni-lj.si

as the Nickel-Manganese-Cobalt- oxide (NMC) used as a demonstration material in this study, exhibit significantly different material properties and are susceptible to a variety of degradation phenomena such as oxygen release[1] and the dissolution of transition metals,[2] formation of rock salt structures,[3] formation of cathode-electrolyte interphases (CEI),[4] cracking of aggregates/secondary particles[5,6] and others. The family of NMC materials also exhibits several intriguing phenomena related to their strong dependence of the diffusion constant on the lithium content in the active material. The group of C. Grey has recently revealed the emergence of the so-called kinetic phase separation, i.e. a spatial non-equilibrium variation of the SOC within single particles[7] and proposed that this phenomenon is caused by the SOC-dependent Li-ion diffusion constant and is also linked to the Li mobility in the bulk material.[8] Moreover, the change in the diffusion constant is particularly remarkable for the highly lithiated particles,[9,10] where the kinetics of Li diffusion becomes much slower.

All these phenomena and the properties of other materials, as well as the design and morphology of the cells and their operating conditions, influence the performance and safety of batteries. Therefore, their adequate performance, durability and safety critically depend on appropriate non-invasive monitoring tools that allow the detection of various in-cell phenomena related to battery performance and degradation. Indeed, such tools can significantly improve battery control and thus safety in real-world applications through a variety of measures such as limiting battery performance, avoiding certain operating conditions, triggering self-healing mechanisms[11] or the battery replacement or other countermeasures. In addition, non-invasive monitoring tools that enable the detection of intra-cell phenomena are also crucial in the battery development process to improve cell design and to provide a feedback loop to material design.

One such powerful method for non-invasive monitoring of intra-cell phenomena is electrochemical impedance spectroscopy (EIS), which is a widely used non-destructive method for characterising electrochemical devices such as Li-ion batteries.[12,13] The main idea of this method is to apply a small potential (potentiostatic EIS or PEIS) or a small current (galvanostatic EIS or GEIS) excitation to the electrochemical device in the form of a sinusoidal perturbation with frequencies ranging across several orders of magnitude[13,14] (typically from kHz to mHz) and measure its response, i.e. amplitude and phase shift. The result is an impedance spectrum presented with a Nyquist diagram that characterises the phenomena in the battery that occur on the different time scales.

Since a typical battery consists of several components and each component leaves its fingerprint in the EIS spectrum,[15,16] deconvoluting the effects of each individual process within the battery cell is a challenging task when interpreting the EIS spectrum. There are still many nonaligned interpretations of the EIS spectrum in the literature,[13,17] especially in the medium to high frequency range, while for the low frequencies it is generally recognised that the EIS spectrum provides profound information about transport phenomena in the active material. The requirement for a correct interpretation is crucially linked to the ability to decipher the contribution of specific performance and degradation related phenomena to the overall EIS spectrum. This requirement is, therefore, inherently interlinked with an adequate model used to interpret the spectra. This requires an adequate physical basis of the model for more detailed analyses and, above all, the determination of realistic values for the model parameters.

There are many publications in the literature[18–20] that analyze the EIS spectra with the electrical circuit representation of the battery, i.e. with the so-called equivalent circuit models (ECMs), which consist of electrical components such as resistors and capacitors and in many cases also of constant phase elements (CPE)[21,22] or finite space Warburg elements.[23–25] Despite the fact that there exist ECMs which feature physicochemical consistency, e.g.[14,26] most of ECMs, e.g.[18–20] do not feature physicochemical consistency and they feature relatively simple model topology. These models have the advantage of being easy to implement and parameterise and require little computational effort. However, they generally do not provide a direct correlation between the model parameters, featuring realistic values, and physicochemical processes in batteries and may also be degenerate.[27] In particular, CPEs are notorious for lacking a physical basis,[28] although they are widely used for fitting the tilted low-frequency parts of the EIS spectrum corresponding to the transport of Li within the electrode material. Only recently, Lasia[29] has indicated potential explanation for CPE phenomena involving the electrosorption diffusion of anions.

With the emergence of the artificial intelligence (AI) based approaches, there are also several publications that apply these approaches for extraction of parameters or states of the electrochemical devices. Babaeiyazdi et al.[30] estimated SoC using machine learning algorithms from the EIS measurements. Pradyumna et al.[31] combined EIS measurements with convolutional neural network to estimate the remaining capacity. Recently, Liu et al.[32] proposed a new method for automatic feature extraction from EIS measurements that combines variational autoencoders and bidirectional gated recurrent unit. The shortcomings of AI-based approaches are usually attributed to the dependence on large, high-quality data sets for training and the difficult interpretation of the underlying physical processes due to the nature of these models.

On the other side of the battery modelling spectrum, there are the physics-based continuum models inspired by the pioneering work of Newman and co-workers[33,34] followed by a number of research models, e.g.[35–40] that are based predominantly on the pseudo-two-dimensional (P2D) approach[41] and validated with the discharge curves. Simplified variants of these models are so-called linearised electrochemical models[42–45] and represent a common approach for modelling EIS spectra. The advantage of these models lies in the fact that the impedance can be derived analytically and the fitting can be done directly in the frequency domain[42,43] with some additional assumptions, e.g. using constant material properties such as solid and ionic conductivity and diffusion constants. However, this is not fully consistent with real experiments, where measurements are conducted in the time domain and Nyquist plots only represent post-processed data. Measurements have to also be conducted under favourable signal-to-noise ratios with sufficiently high amplitude of the excitation signals. Therefore, until now, frequency domain models were subjected to several limitations when interpreting EIS spectra of NMC materials, in particular at higher lithiation levels, where the diffusion constant exhibits strong dependency on the level of lithiation.[9,10] This becomes even clearer when it comes to deciphering the contributions of various phenomena in the low-frequency EIS spectrum, as a non-negligible amount of charge, e.g. in GEIS measurements, is transferred at low frequencies. In addition to the diffusion constant, the surface concentration and thus also the chemical potential and OCV of the material changes during such experiments. Previous studies have already reported that variations in solid-phase diffusion constant and OCV have a non-negligible influence on the EIS spectra.[46]

More advanced models, of which there are not many in the literature, model the EIS spectra with the full electrochemical models in the time domain corresponding to real experiments. One such work is by R-Smith et al.[47] in which they modelled the EIS spectra with COMSOL Multiphysics of the full commercial cell at different degradation levels and extracted several ageing parameters, supported by advanced microscopy techniques. In addition, Xie et al.[48] studied effects of cycling on the impedance response of the Li-ion battery using multiphysics-based EIS simulation. Reformulated P2D has also been used for the simulation of the EIS spectra, e.g. Pathak et al.[49] presented a hybrid analytical-collocation approach for the fast simulation of the impedance response for a Li-ion battery using the P2D model. Teo et al.[50] simulated the dynamic electrochemical impedance response of full Li-ion cell during charging and discharging using the P2D model using a computationally efficient approach and Murbach et al.[51] extended the P2D model to evaluate the linear and nonlinear response of the full Li-ion cell.

These models have in common that they model the EIS spectra of the full-cell configurations with the standard set of Newman-based governing equations, which include standard transport and potential equations, a charge transfer model and a corresponding double-layer model for the electrode material.[37,48,52] The results generated with

these models feature a single high-frequency semicircle and a tilted low-frequency tail. Such behavior can indeed, in general, be qualitatively observed in many experimentally measured EIS spectra, e.g.[53–55] These spectra appear, at a first glance, as simplistic Nyquist plots, but the collective behavior of both electrodes in the full-cell systems results in an EIS spectrum that is a superposition of a number of intra-cell phenomena occurring on similar time scales. Resultantly, these apparently simplistic Nyquist spectra indeed mask several phenomena occurring at similar time scales, hence, making their model supported deciphering very challenging. These phenomena range from solid-phase diffusion in the electrode particles, diffusion in the electrolyte phase (porous electrodes and separator), interfacial electrochemical reactions and contact resistances in both electrodes[16] to various impedance contributions due to battery degradation.[47]

This challenge can be circumvented by using custom-made half-cells in this work. We have designed these half-cells (details of which can be found in appendix Section Experimental) in a way that specific underlying phenomena in such a half-cell occur at different time scales, thus allowing the detection of phenomena that are often hidden or superimposed in the full-cell experiments, but are important for the operation of the cell and thus important to be modelled. In summary, the currently published Newman-based models are not capable to virtually replicate relevant intra-cell phenomena with physically meaningful values of model parameters compared to the model proposed in this paper because, as will be shown later in the paper, they lack submodels of specific phenomena that are crucial for modelling multiple semicircles characteristic of specific intra-cell phenomena.

In order to overcome the above challenges related to deciphering the phenomena contributing to the overall shape of the EIS spectrum, we present a first time-domain based electrochemical model, validated on the tailor made half-cell over a wide range of frequencies. This was made possible by originating from an advanced modelling framework presented in previous references,[56–58] which has been significantly extended to comply with the objective to virtually replicate EIS results with high fidelity and physically meaningful parameters. This means that it is capable of modelling three superimposed high-frequency semicircles, which are inherent to specific intra-cell phenomena, as well as tilted diffusion tail at low-frequencies. These advanced modelling capabilities include significant extensions i.e. sub-models, namely the double layer phenomenon related to the carbon black/electrolyte interface, the double layer phenomenon at the metal-Li anode/electrolyte interface, and transport of charged species through the discretised porous solid electrolyte interphase (SEI) layer placed between the separator and the Li-anode. The results of the model demonstrate that additional double-layer phenomena at the carbon black/electrolyte interface, the effect of introducing the particle size distribution to the slope of the EIS spectrum in the low-frequencies (one of the possible explanations/compensations for the CPE elements) and the effect of diffusivity of charged species through the SEI layer on the EIS spectra are crucial to properly decipher the underlying phenomena and to predict physically meaningful values of the model parameters.

Results, in addition, reveal a significant impact of the need for a sufficiently high discretisation resolution, which significantly impacts results of the EIS spectra and, thus, impact values of the material properties when extracted from the EIS spectra. We also provide detailed and consistent root-cause explanations. Supported by the non-invasive EIS measurements, the presented high fidelity model can be considered as a tool for advanced characterization of the intra-cell parameters and states of the battery and be used as a virtual sensor in next-generation battery management systems.

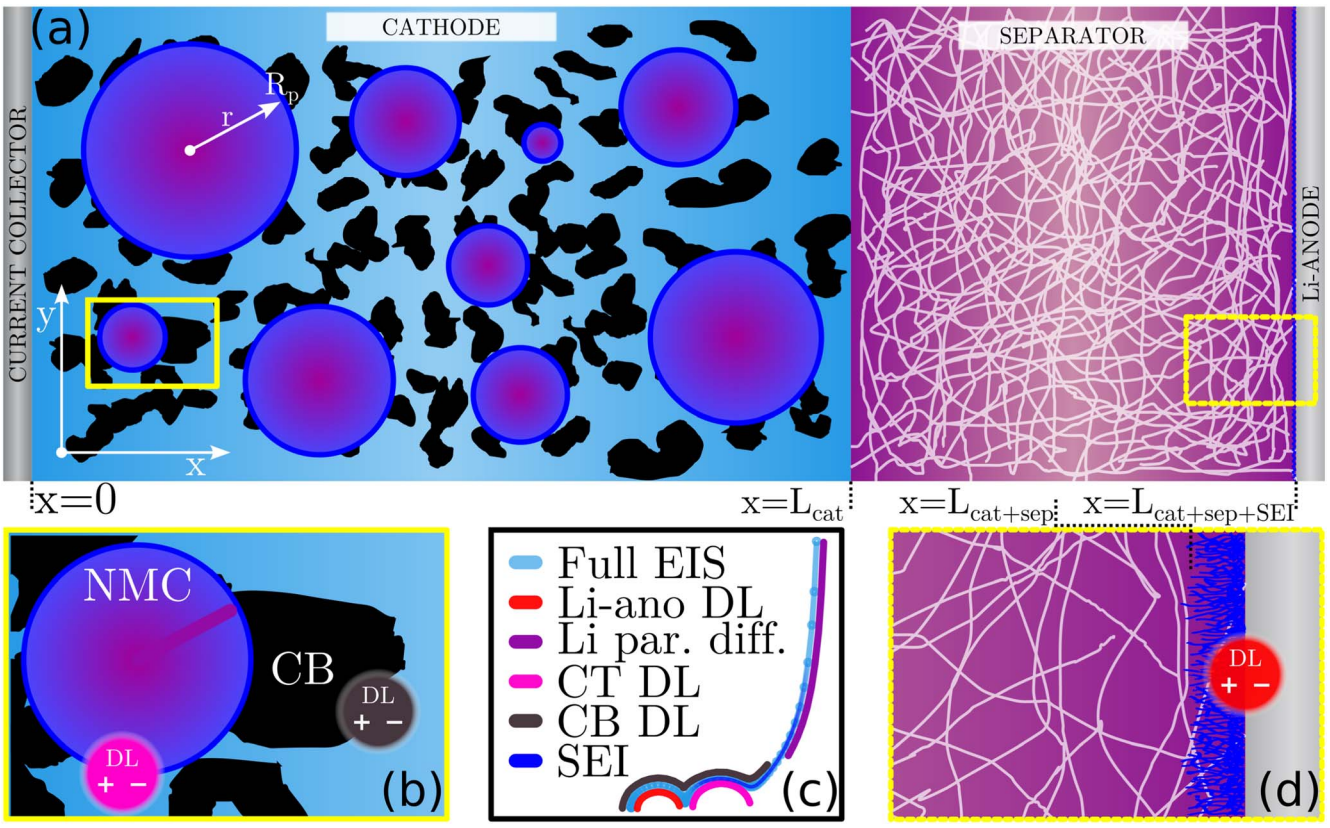

Figure 1. (a) A schematic representation of the modelling domain, i.e. half-cell configuration including the cathode with electrode particles and carbon black, the porous separator, the porous SEI layer and the Li counter anode; (b) a detailed scheme of a single representative particle surrounded by the electrolyte (light blue color) and the carbon black and emergence of the double layer at the interface between the solid (particle and carbon black) and the liquid phase, denoted by pink and gray circles with +/ − symbols; (c) indicated contributions of individual phenomena to the full EIS spectra namely the three double layer models, the transport of Li within the particle and the transport of Li^+ through the porous SEI layer, the color coding of the individual phenomena refers to the subfigures (b) and (d); (d) representation of the porous SEI layer and the double layer phenomena at the Li-anode interface denoted by red circle with +/ − symbols.

The following Sections are organised as follows. Section Battery Model presents the governing equations of the developed model and Section Results presents the validation of the calculated EIS spectra in the time-domain versus the experimentally measured ones and impact of certain sub-models or parameters on the spectrum. The appendix presents the experimental measurements supporting the simulation results, the numerical approaches, the parameters used in the simulations and the corresponding parameter sensitivity analysis.

Battery Model

This Section presents the governing equations of the model and the corresponding boundary conditions, which are based on our previous publications[56–58] and have been extended by several sub-models discussed in this section. To complement the equations, a schematic representation of the modelling domain and the most important models can be seen in Fig. 1.

Governing equations.—The following assumptions were made in the presented model when dealing with low current and voltage amplitudes during the EIS procedure: the active electrode material, i.e. secondary particles, is modelled as a spherical particle, which is a reasonable approximation of the NMC material,[59] the electrode material is ideally immersed in the electrolyte, which is the case for dilute electrodes (Fig. A·1), the volume change of the electrode material during (de)intercalation is neglected. This is a common assumption for batteries with liquid electrolyte, while this simplification can be considered valid for the diluted electrodes analysed in this work. The electrode material exhibits a monotonous dependence of the chemical potential on the stoichiometry of the particles, while parameters such as temperature, transference number, activity coefficient, diffusion constant and conductivity of the electrolyte were kept constant due to the negligible temperature, concentration and potential gradients and their respective absolute fluctuations over the half-cell. Although these dependencies are available in the model[56–58] they were switched-off reduce the influence of parameters with negligible effect.

The transport and mass balance of the charged species (Li-ions in this case) in the electrolyte is governed by the following equation

$$\frac{\partial(\epsilon_e c_e)}{\partial t} = \nabla\cdot\left(D_e^{\text{eff}}\nabla c_e - \frac{t_+}{z_+F}i_e\right) - a_{es}(j_{es} - j_{es}^{DL}) + a_{ecb}\, j_{ecb}^{DL}, \quad [1]$$

where the first term $D_e^{\text{eff}}\nabla c_e$ represents the diffusion flux of the charged species with the effective diffusion constant governed by the Bruggeman relation $D_e^{\text{eff}} = D_e(c_e)\epsilon_e^{\text{brugg}}$[60,61] with ϵ_e representing porosity of the electrode, the second term $\frac{t_+}{z_+F}i_e$ represents the migration term[62] which is dependent on the liquid-phase current density i_e and is defined in the Eq. 3, t_+ and z_+ represent the transference number and the charge of the species, respectively, a_{es} and a_{ecb} represent specific surface of the electrode material and the carbon black in the electrode, respectively, and finally j_{es} represents reaction rate of the electrochemical reaction at the electrode material/electrolyte interface (Eq. 9), j_{es}^{DL} represents reaction rate due to double-layer effects at the electrode material/electrolyte interface (Eq. 13) and j_{ecb}^{DL} represents reaction rate due to double-layer effects at the carbon black/electrolyte interface (Eq. 14). Additional terms from double-layer phenomena ensure mass conservation in the system. The last two terms in the Eq. 1 are not relevant for the separator region of the modelling domain.

Under assumption of electro-neutrality[36] over the modelled half-cell (Fig. 1a), one can write the following equation

$$\nabla\cdot i_e + \nabla\cdot i_s = 0, \quad [2]$$

where besides previously mentioned i_e, the i_s represents solid phase current density.

Liquid-phase potential Φ_e is governed by charge leaving or entering the liquid phase, and can be written as

$$\begin{aligned}\nabla\cdot i_e &= \nabla\cdot\left(-\kappa_e^{\text{eff}}\nabla\Phi_e + 2\frac{\kappa_e^{\text{eff}}RT}{F}(1-t_+)\left(1+\frac{\partial\ln f_\pm}{\partial\ln c_e}\right)\nabla\ln c_e\right)\\ &= -F(a_{es}(j_{tot} - j_{es}^{DL}) - a_{ecb}\, j_{ecb}^{DL}),\end{aligned} \quad [3]$$

where κ_e^{eff} represents the effective liquid-phase conductivity evaluated from the Bruggeman relation $\kappa_e^{\text{eff}} = \kappa_e(c_e)\epsilon^{\text{brugg}}$, $f_\pm$represents the activity coefficient[63] and finally, F, R and T are the Faraday's constant, the gas constant and the temperature, respectively.

Similarly to Eq. 3, the solid phase potential Φ_s is governed by the charge leaving or entering the solid phase, and can be written in the form of Ohmic law as

$$\nabla\cdot i_s = \nabla\cdot(\sigma_s^{\text{eff}}\nabla\Phi_s) = F(a_{es}(j_{tot} - j_{es}^{DL}) - a_{ecb}\, j_{ecb}^{DL}). \quad [4]$$

The effective solid phase conductivity σ^{eff} is calculated as $\sigma^{\text{eff}} = \sigma(1-\epsilon_e-\varphi^{\text{V,b+cb}})$, where $\varphi^{\text{V,b+cb}}$ represents the combined volume fraction of binder and carbon black.

The transport and mass balance of Li in the electrode material is determined by the general form of the diffusion equation where the Li distribution is determined by the gradient of the chemical potential μ and is written as follows

$$\frac{\partial c_s}{\partial t} = \nabla\cdot\left(\frac{D_s(c_s)c_s}{RT}\nabla\mu(c_s)\right), \quad [5]$$

where c_s and D_s represent the solid-phase concentration and the diffusion constant of Li in the electrode material, respectively. Assuming spherical electrode particles, the Eq. 5 can be rewritten to the following form

$$\begin{aligned}\frac{\partial c_s}{\partial t} &= \frac{1}{r^2}\frac{\partial}{\partial r}\left(r^2\frac{D_s(c_s)c_s}{RT}\frac{\partial\mu(c_s)}{\partial r}\right)\\ &= \frac{1}{r^2}\frac{\partial}{\partial r}\left(r^2\frac{D_s(c_s)c_s}{RT}\frac{\partial\mu(c_s)}{\partial c_s}\frac{\partial c_s}{\partial r}\right),\end{aligned} \quad [6]$$

where r represents the radial coordinate in the electrode material domain. For the concentration dependent chemical potential, the following expression was used

$$\mu(c_s) = RT\ln\left(\frac{c_s}{c_{s,\text{ref}}}\right), \quad [7]$$

where $c_{s,\text{ref}}$ represents a reference solid-phase concentration. Inserting expression for chemical potential from Eq. 7 into the Eq. 5 leads to a well known Fick's diffusion equation for the transport of Li in spherical particles

$$\frac{\partial c_s}{\partial t} = \frac{1}{r^2}\frac{\partial}{\partial r}\left(D_s(c_s)r^2\frac{\partial c_s}{\partial r}\right). \quad [8]$$

However, the modelling framework is designed to allow the inclusion of arbitrary chemical potential expressions by directly solving the Eq. 6, including non-monotonic chemical potentials characteristic of phase-separating materials.[56]

The charge transfer reaction on the surface of the electrode particles (electrolyte/solid interface) is modelled with the widely used Butler-Volmer equation[36,64,65]

$$j_{es} = \frac{i_{0,es}}{F}\left[\exp\left(-\frac{\alpha_c F}{RT}\eta_{es}\right) - \exp\left(\frac{(1-\alpha_a)F}{RT}\eta_{es}\right)\right], \quad [9]$$

Table I. Lithiation level and corresponding open circuit voltage (OCV) of the NMC811 material obtained from measurements shown in Fig. A·2.

x [mol]	OCV [V]
0.338	4.055
0.551	3.805
0.747	3.665

where $i_{0,es}$ is the stoichiometry-dependent exchange current density, α is the charge transfer coefficient for the cathodic and anodic reaction, and η_{es} is the overpotential for the electrochemical reaction and is calculated using the following equation

$$\eta_{es} = (\Phi_s - \Phi_e) - U^{OCV}. \quad [10]$$

The last term in Eq. 10 represents the stoichiometry-dependent open circuit voltage (OCV). In this work, the OCV of the NMC811 cathode material vs. Li/Li^+ was determined using the GITT experiment (Section Electrochemical measurements). Similar to the Eq. 9, the electrochemical reaction at the electrolyte/Li-anode interface (Fig. 1b) is also modelled with the Butler-Volmer equation[66]

$$j_{eLi} = \frac{i_{0,eLi}}{F}\left[\exp\left(-\frac{\alpha_c F}{RT}\eta_{eLi}\right) - \exp\left(\frac{(1-\alpha_a)F}{RT}\eta_{eLi}\right)\right], \quad [11]$$

with $i_{0,eLi}$ and η_{eLi} are the exchange current density and the overpotential at the electrolyte/Li-anode interface. The overpotential η_{eLi} is defined as

$$\eta_{eLi} = (\Phi_s - \Phi_e) - U_{Li}^{OCV}, \quad [12]$$

where the open circuit voltage of the Li-anode is set as constant $U_{Li}^{OCV} = 0.0$ V.[67]

As already announced in the discussion of the Eq. 1, the modelling framework also contains several models of double-layer phenomena at different locations in the modelling domain and follows the widely adopted formulation from Ong et al.[34] The reaction rate j_{es}^{DL} due to the double-layer effect on the surface of the electrode particles (electrolyte/solid interface, Fig. 1b) is calculated as

$$j_{es}^{DL} = C_{es}^{DL}\frac{\partial(\Phi_s - \Phi_e)}{\partial t}, \quad [13]$$

where C_{es}^{DL} represents the capacitance of the double-layer on the surface of the electrode particles. Another double-layer effect is modelled at the surface of the carbon black (Fig. 1b) which is in contact with the electrolyte

$$j_{ecb}^{DL} = C_{ecb}^{DL}\frac{\partial(\Phi_s - \Phi_e)}{\partial t}, \quad [14]$$

where C_{ecb}^{DL} represents the capacitance of the double-layer of the carbon black. The last double-layer phenomena is modelled at the electrolyte/Li-anode interface (Fig. 1d) and is evaluated as

$$j_{eLi}^{DL} = -C_{eLi}^{DL}\frac{\partial\Phi_e}{\partial t}, \quad [15]$$

where C_{eLi}^{DL} represents the capacitance of the double-layer on the Li-anode foil in contact with the electrolyte and solid-phase potential Φ_s is set to be 0.0 V. The Eq. 15 enters into the Eqs. 21 and 25 as a boundary condition at the interface.

Finally, the porous SEI layer that forms on the surface of the Li-anode was also modelled. The thin layer was spatially discretised, similar to the electrode an the separator. To account for the additional contribution of the diffusion impedance of the charged species through the porous SEI, the transport and mass balance equation can be written as a simplified version of the Eq. 1

$$\frac{\partial(\epsilon_e^{SEI} c_e)}{\partial t} = \nabla\cdot\left(D_e^{eff,SEI}\nabla c_e - \frac{t_+}{z_+ F} i_e\right), \quad [16]$$

where ϵ_e^{SEI} is the porosity of the porous SEI layer and $D_e^{eff,SEI}$ represents the effective diffusion constant of the charged species through the SEI layer which is calculated again by the Bruggeman relation $D_e^{eff,SEI} = D_e^{SEI}(\epsilon_e^{SEI})^{brugg}$.[60,61] The Eq. 16 does not contain any source/sink terms, as the experiments were carried out with fresh cells without long-term cycling, as ageing effects are not within the scope of this work. In addition to the concentration, the liquid-phase potential Φ_e in the porous SEI layer was also modelled using the following equation

$$\nabla\cdot i_e = \nabla\cdot\left(-\kappa_e^{eff,SEI}\nabla\Phi_e + 2\frac{\kappa_e^{eff,SEI}RT}{F}(1-t_+)\left(1 + \frac{\partial\ln f_\pm}{\partial\ln c_e}\right)\nabla\ln c_e\right) = 0, \quad [17]$$

where $\kappa_e^{eff,SEI}$ represents the conductivity of the effective liquid-phase in the porous SEI layer and is evaluated from the Bruggeman relation $\kappa_e^{eff,SEI} = \kappa_e(\epsilon_e^{SEI})^{brugg}$.

Boundary conditions.—This Section presents the boundary conditions used in the computational domain analysed in this paper. They are organised according to the corresponding governing equations presented above. The coordinates of the individual boundary conditions are shown schematically in Fig. 1.

Electrolyte concentration.—The following boundary conditions are imposed for the transport and mass balance of the charged species in the electrolyte governed by Eq. 1. The zero-flux boundary conditions are imposed at the current collector/cathode boundary:

$$-D_e^{eff}\nabla c_e|_{x=0} = 0. \quad [18]$$

Continuous flux boundary conditions are imposed inside the cell:

$$-D_e^{eff}\nabla c_e|_{x=L_{cat,-}} = -D_e^{eff}\nabla c_e|_{x=L_{cat,+}}, \quad [19]$$

$$-D_e^{eff}\nabla c_e|_{x=L_{cat+sep,-}} = -D_e^{eff}\nabla c_e|_{x=L_{cat+sep,+}}. \quad [20]$$

The reaction rate j_{eLi}, which acts as a source of Li-ions into the computational domain, and reaction rate j_{eLi}^{DL} due to the double-layer phenomena are imposed at the Li-anode boundary:

$$-D_e^{eff,SEI}\nabla c_e|_{x=L_{cat+sep+SEI}} = \frac{-j_{eLi} + j_{eLi}^{DL}}{F}. \quad [21]$$

Electrolyte potential.—The following boundary conditions are imposed for the Eq. 3 that governs liquid-phase potential Φ_e of the charged species in the electrolyte. Similar to the Section Electrolyte concentration, Zero-flux boundary conditions are imposed at the current collector/cathode boundary:

$$-\kappa_e^{eff}\nabla\Phi_e|_{x=0} = 0. \quad [22]$$

Continuous flux boundary conditions are imposed inside the cell:

$$-\kappa_e^{eff}\nabla\Phi_e|_{x=L_{cat,-}} = -\kappa_e^{eff}\nabla\Phi_e|_{x=L_{cat,+}}, \quad [23]$$

$$-\kappa_e^{eff}\nabla\Phi_e|_{x=L_{cat+sep,-}} = -\kappa_e^{eff}\nabla\Phi_e|_{x=L_{cat+sep,+}}. \quad [24]$$

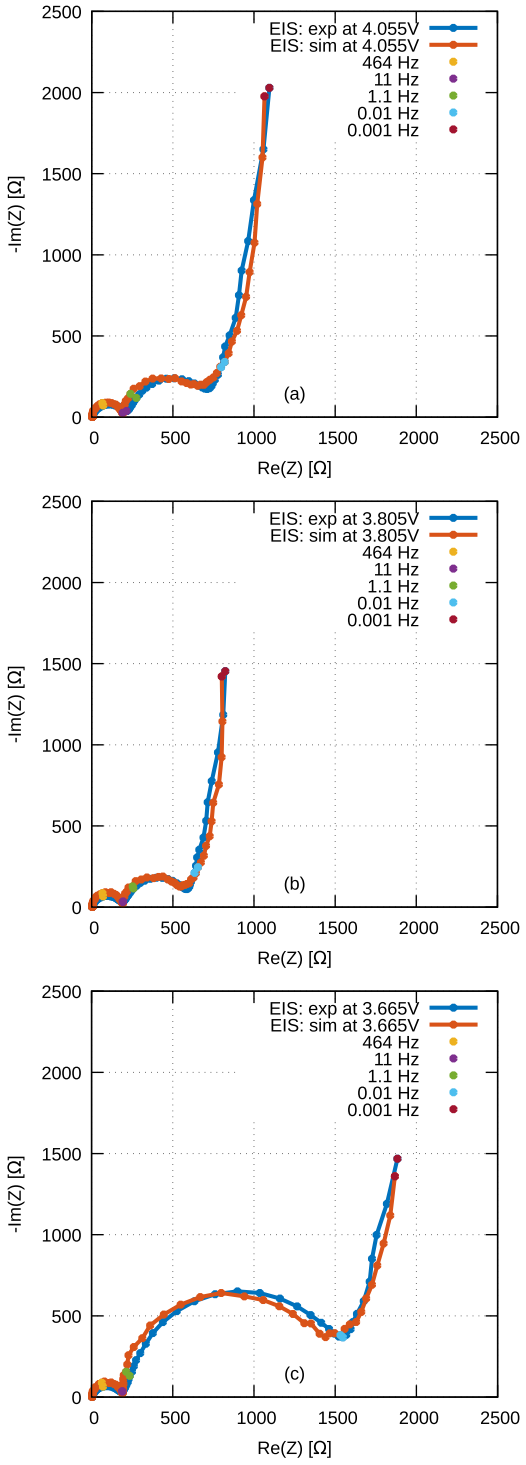

Figure 2. A comparison between experimentally measured and simulated EIS spectra at different degrees of lithiation corresponding to the following open-circuit voltages: (a) 4.055 V; (b) 3.805 V; and (c) 3.665 V. To improve comparison, the positions of five selected frequencies over several orders of magnitude in the spectra are marked with the different coloured dot symbols.

The reaction rates j_{eLi} and $j_{\mathrm{eLi}}^{\mathrm{DL}}$ are again imposed at the Li-anode boundary:

$$-\kappa_{\mathrm{e}}^{\mathrm{eff}}\nabla\Phi_{\mathrm{e}}|_{x=L_{\mathrm{cat+sep+SEI}}} = -j_{\mathrm{eLi}} + j_{\mathrm{eLi}}^{\mathrm{DL}}. \quad [25]$$

Solid phase potential.—The following boundary conditions are imposed for the governing Eq. 4 that governs the solid phase potential Φ_{s}. The applied (dis)charge current density I_{app} is imposed at the current collector/cathode boundary condition:

$$-\sigma^{\mathrm{eff}}\nabla\Phi_{s}|_{x=0} = I_{\mathrm{app}}. \quad [26]$$

The zero-flux boundary condition is imposed at the cathode/separator boundary since no electric current is supposed to flow into the separator domain:

$$-\sigma_{\mathrm{s}}^{\mathrm{eff}}\nabla\Phi_{\mathrm{s}}|_{x=L_{\mathrm{cat}}} = 0. \quad [27]$$

Electrode particle concentration.—Assuming spherical particles, the solution of the Eq. 6 requires two boundary conditions for the solid-phase concentration c_{s} in the electrode particle. The boundary condition of zero flux is applied in the centre of the electrode particle:

$$-D_{\mathrm{s}}\nabla c_{\mathrm{s}}|_{r=0} = 0, \quad [28]$$

whereas on the surface of the particle the reaction rate is predetermined due to the electrochemical reaction

$$-D_{\mathrm{s}}\nabla c_{\mathrm{s}}|_{r=R_{\mathrm{p}}} = j_{\mathrm{es}}. \quad [29]$$

Results

In this section, the results of the proposed modelling framework validated with the experimental measurements are presented, followed by the variation of additional parameters to investigate their effects on the EIS spectra.

Experimental validation.—The model was validated with the experimentally measured EIS spectra on the laboratory built half-cell with the electrode material NMC811. Details on the experimental electrode preparation, cell assembly and the electrochemical measurements can be found in the appendix Section Experimental.

The starting point for the model validation with the experiments were raw measurement data points consisting of frequency, real and complex part of the impedance which were imported into the model. Three EIS curves were measured at three different voltage levels (see Table I). For each frequency, galvanostatic sinusoidal excitation was used as a boundary condition at the current collector/cathode boundary (Eq. 26) with an amplitude of C/10^4 to ensure a linear response without higher harmonics[13] and a duration of 20 periods with 10^4 time-steps within each period for accurate results. From the last period, the amplitude of the voltage response and the phase shift between the sinusoidal current and voltage time traces were extracted. Based on this information, the real and complex parts of the impedance for a single frequency were calculated.

After completing the simulations for each frequency, the root-mean-square deviation (RMSD) between the experimental measured values and the simulated values was determined. The RMSD value was then entered into to the self-implemented evolutionary algorithm called Differential evolution proposed by Storn and Price[68] which performed an optimisation of the problem by minimising the total RMSD value (i.e. the sum of the individual RMSD values for all three cases and all frequencies) by iteratively improving set of fitting parameters. The parameters that were fitted are as follows: exchange current density $i_{0,\mathrm{es}}$ and $i_{0,\mathrm{eLi}}$ from Eqs. 9 and 11, respectively, double layer capacitances $C_{\mathrm{es}}^{\mathrm{DL}}$, $C_{\mathrm{ecb}}^{\mathrm{DL}}$ and $C_{\mathrm{eLi}}^{\mathrm{DL}}$ from the Eqs. 13, 14 and 15, solid-phase diffusion constant D_{s} from Eq. 8, specific surface of the carbon black a_{ecb} from Eqs. 1, 3 and 4, the diffusion constant of the Li-ions through the porous SEI layer at the Li-anode $D_{\mathrm{e}}^{\mathrm{SEI}}$ from Eq. 16 and finally the number of representative electrode particles was fitted. The size of the electrode particles was determined using a Gaussian distribution according to the manufacturer's size specification in Table A·I and SEM images of a pristine electrode material. The specific surface of the carbon black a_{ecb} was

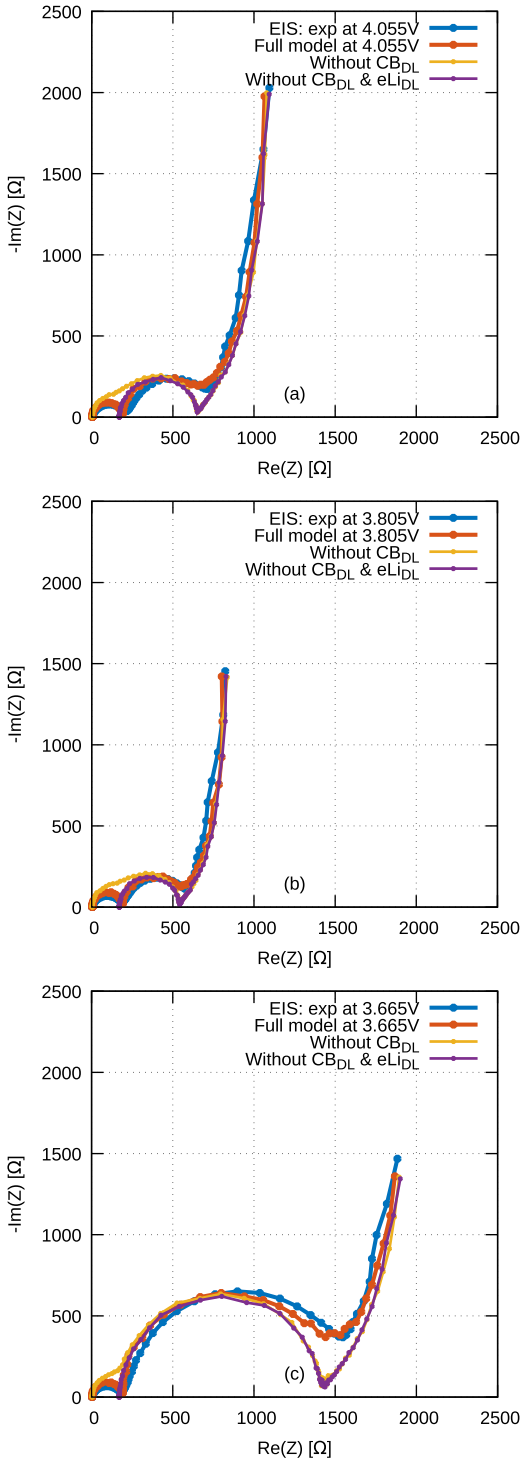

Figure 3. A comparison between experimental and full model EIS results from Fig. 2 with the modelling results of the model without the double layer model at the carbon black/electrolyte interface and at the metal-Li anode/electrolyte at different degrees of lithiation corresponding to the following open-circuit voltages: (a) 4.055 V; (b) 3.805 V; and (c) 3.665 V.

fitted due to the fact that not all the surface of the carbon black is exposed to the electrolyte. Of the above fitting parameters, only the exchange current density $i_{0,es}$ and solid phase diffusion constant D_s were fitted separately for each case to account for the dependency of the $i_{0,es}$ and D_s to the different degrees of lithiation in the NMC material,[10,16] whereas the other fitting parameters were kept constant for all three cases in Fig. 2. For this validation, we discarded the commonly used parabolic ansatz before the exponential parts of the Butler-Volmer equation. Therefore, the entire pre-exponential term was fitted as a single parameter due to the fact that the ansatz qualitatively captures the dependence of the exchange current density to the lithiation level at the particle's surface.[16] Furthermore, we assumed constant solid-phase diffusion constant due to negligible change in transferred charge during the galvanostatic EIS excitation for each EIS measurement (Table I).

Figure 2 shows the comparison between measured and simulated EIS spectra (calculated with the minimisation of the RMSD value) at three different cell voltages corresponding to three different degrees of lithiation, i.e. stoichiometries, of the NMC material (see Table I). In addition, five selected frequencies are labelled in each of the two EIS curves (measured and simulated) to illustrate their relative position on both spectra, as the Nyquist plot does not explicitly present the frequency information.

The resulting simulated EIS spectra show good agreement with the experimentally measured spectra over a wide frequency range from 100 kHz to 1 mHz. Some important aspects from Fig. 2 that support the model's capabilities to model EIS spectra with a good accuracy, that exceeds that of other models analysed in the Introduction, are worth mentioning.

Firstly, it is important to emphasise that the model is capable to model smaller semi circle at the highest frequencies, i.e. Re(Z) approximately between 3 Ω and 250 Ω. Its occurrence is due to the electrochemical reaction and the double layer effects at the separator/SEI/Li-anode interface[16] (Fig. 1d and Eqs. 11 and 15). This statement is supported by the fact that the impedance of the semi circle remains nearly constant for all three case which further confirms the adequacy and capability of the included sub-models at the Li-anode interface.

The second semi circle, also known as the charge transfer (CT) semi circle, in the medium frequency range is due to electrochemical reaction and double layer effects at the particle's surface[16,28] (Fig. 1b and Eqs. 9 and 13). The impedance of this semi circle changes significantly between the three cases, with the largest change occurring at the lowest voltage (Fig. 2c), i.e. for the most lithiated NMC material of the three cases. The change in impedance correlated directly with the change in exchange current density $i_{0,es}$ in Eq. 9, which was fitted separately for each case, as $i_{0,es}$ depends on the surface stoichiometry of the electrode particles.

The transition from the charge transfer semi circle to the diffusion tail occurs in the analysed case at -Im(Z)>0 for all three experimental EIS spectra. The same phenomenon can also be observed in the literature.[53–55] In special cases, as for example single electrode particle and micro-electrode technique[69] without the use of carbon black, this transition occurs near the Re(Z) axis. However, we identified this transition to be a consequence of the double layer phenomena at the electrolyte/carbon black interface, which required inclusion of the novel carbon black double layer model in the electrochemical model (Fig. 1 and Eq. 14). This model is missing in the standard set of Newman-based governing equation and, hence, in the models from the literature.[35–40] The obtained value from the minimisation algorithm of the carbon black double layer capacitance $C_{ecb}^{DL} = 5.74\mu F/cm^2$ (or 0.0574 F/m^2 in the Table A·I) shows a very good agreement with the experimental determination of specific double-layer capacitance due to carbon black conductive additive presented in appendix Section Experimental determination of specific double-layer capacitance due to carbon black conductive additive and in the Fig. A·4, which confirms the addition of the novel model. As shown later in the Fig. 4, the elevated transition can indeed still be modelled with reasonable accuracy, but at the cost that the values of other parameters have to be compensated for and thus become unphysical, confirming once again the need to include the carbon black double layer model. Such addition (Section Impact of novel submodels to the EIS spectra), which consistently represents the effects at the electrolyte/carbon black additive interface, makes possible simulating

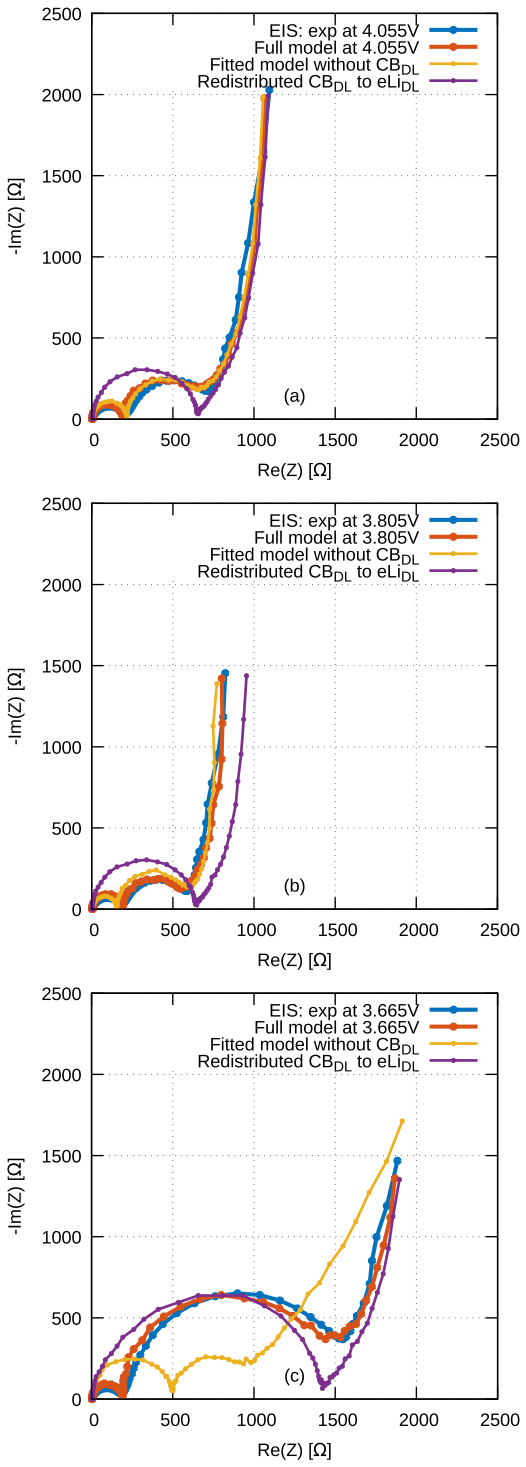

Figure 4. A comparison between experimental and full model EIS results from Fig. 2 with the fitted results of the model without the double layer model at the carbon black/electrolyte interface and with the model with the redistributed carbon black capacitance to the capacitance of the double layer at the Li-anode. The simulations were performed at different degrees of lithiation corresponding to the following open-circuit voltages: (a) 4.055 V; (b) 3.805 V; and (c) 3.665 V.

experimentally observed transitions from the charge transfer semi circle to the diffusion tail at -Im(Z)>0 and the obtaining of realistic model parameters, and thus, represents a meaningful and innovative extension of the standard set of Newman-based governing equation.

The diffusion tail, which is due to the to the transport of Li within the electrode particles, corresponds to the low frequency diffusion impedance.[16,28] In this frequency range there are two important aspects, that need to be emphasised. The first is the challenge of modelling the tilt in the diffusion tail and the second is the agreement between measured and simulated values of the complex impedance at the lowest frequencies. The tilt proved to be challenging to model without the use of the CPE elements, e.g.[16] and with a single representative averaged sized particle which most of the P2D electrochemical models in the literature still use, e.g.[37,48,52] In this work, we propose the inclusion of number of differently sized representative particles in the electrode, which further enhances consistency between the modelled and experimental system. This functionality leads to combining different eigen diffusion time constants to achieve a reasonable tilt in the diffusion tail, that is characteristic of the measured spectra. This approach is also supported by the experimental work of Wu et al.[70] in which they demonstrated impact of the different particle size distributions on the EIS spectra. As discussed in the Introduction, the particle size distribution might be one of the possible explanations for the tilt, but we do not claim that is the only one. Diffusion impedance of charged species through the SEI layer at the Li-anode interface might also contribute to the mid to low frequency parts of the EIS spectra, i.e. transitioning from the charge transfer semi circle to the diffusion tail as indicated in Fig. 1. Later in the Fig. 5 we demonstrate that a single particle of average size cannot replicate the tilt in the diffusion tail and additionally, in Figs. 6 and A·5 we demonstrate the potential impact of the hindered diffusivity of charged species through the SEI layer on the increase of impedance in the EIS spectra. Knowledge of the size distribution of the electrode materials used in the cell (see size distribution data in Table A·I) plays another crucial role in physically based models. The third aspect regarding the diffusion tail is the agreement between measured and simulated values of the complex impedance at the lowest frequencies, which in all cases show a very good agreement with very small deviations. According to the analytical derivations the impedance of the single particle model impedance by Meyers et al.[46] the "height" of the imaginary/complex impedance at the lowest frequencies depends on the local gradient of the OCV with respect to the actual degree of lithiation. It is therefore important to emphasise here that an accurate OCV measurement (Fig. A·2) is crucial for plausible modelling of the EIS spectra.

The presented results show that the proposed model is able to capture the most important features from the experimentally measured EIS spectra, i.e. two distinguishable semi circles, an elevated transition to the low frequency diffusion tail and the tilt of the aforementioned diffusion tail. Based on these facts, the proposed model can be characterised as advancement over the existing models in the field of modelling EIS spectra in the time-domain.

Impact of novel submodels to the EIS spectra.—To further underpin importance of the newly added modelling features, this Section presents the results of a full model and several variants of this model, in which these features were systematically switched off to demonstrate their effects on the EIS spectra.

Figure 3 shows the comparison of the experimental and simulated EIS spectra (from now referred as the "Full model") with the EIS spectrum obtained without the double layer model at the electrolyte/carbon black interface and with the EIS spectrum obtained without the double layer model at the Li-anode interface for the three different OCV voltages as in the previous Fig. 2. The other parameters were kept constant as they were calculated for the Full model.

Switching off the double layer model at the electrolyte/carbon black interface (Fig. 1b and Eq. 14) and retaining the remaining modelling parameters the same, causes the spectrum to approach Re (Z) axis at the transition to the low frequency solid-diffusion impedance tail for all three cases, which is not in agreement with the measurements where this transition is substantially elevated in terms of -Im(Z) values. Furthermore, the high frequency semicircle

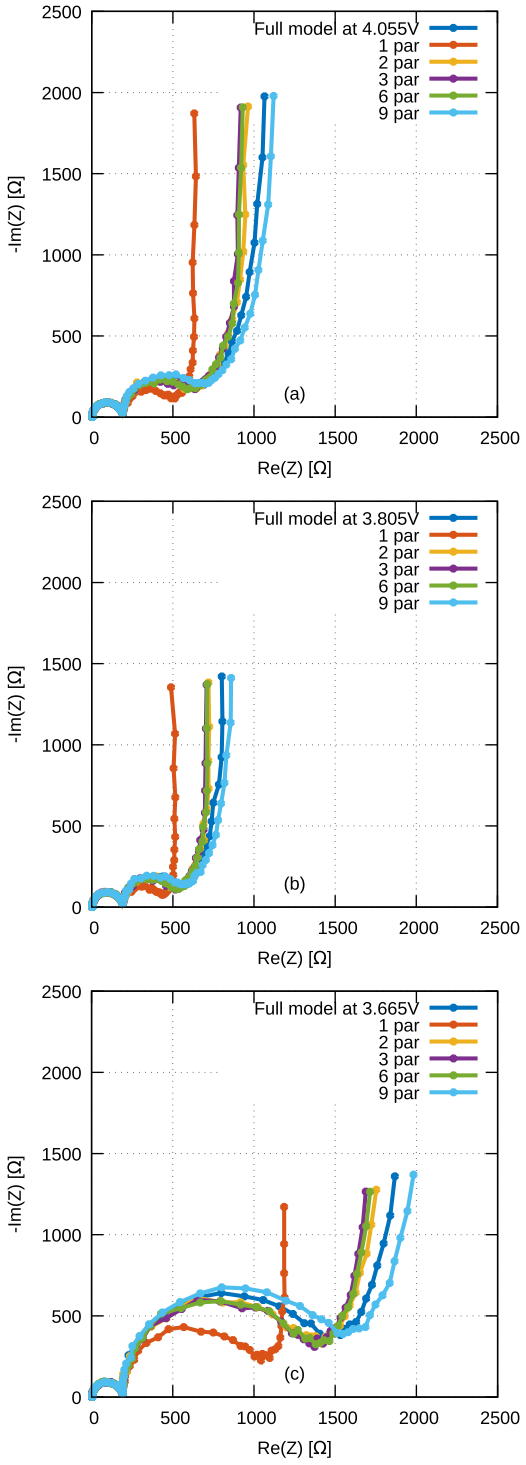

Figure 5. Impact on the EIS spectra when varying number of representative particles in the control volume. Parameters are taken from the full model for all three cases from the Fig. 2 with 12 representative particles used in the simulations.

overlaps with the charge transfer semicircle in all three cases, when double layer effects at the electrolyte/carbon black interface are not taken into account. These results clearly indicate the importance of including the double layer model at the electrolyte/carbon black interface, especially in the cases with higher mass or volume fraction of carbon black.

In addition to switching off the carbon black double layer model, the last purple line in the Fig. 3 represents simulated EIS spectra, where the double layer model at the Li-anode interface is also being switched off (similarly as before, the remaining modelling parameters were kept the same). This has two consequences. Firstly, the first high frequency semicircle disappears completely and secondly, all high frequencies are shifted to the main charge-transfer semicircle. These calculated spectra are consequently entirely misaligned with the experimentally measured spectra. Most importantly, the absence of the double layer model at the Li-anode interface predicts a false internal resistance of the cell in the range of 200 Ω, if the intersection with the Re(Z) axis is considered as a measure of the internal resistance, while in the experiment this value is almost negligible considering the entire EIS spectrum and it is around 3 Ω. The inclusion of all significant high frequency phenomena is, therefore, important for plausible modelling of the EIS spectra.

Based on the results shown in Fig. 3 an important question arises: How well can the electrochemical model fit the parameters to the experimental measurements, if there is no double layer model at the electrolyte/carbon black interface? To answer this question, additional optimisation protocol was applied to the electrochemical model (as in the case of the Full model in Fig. 3), but without the aforementioned double layer model at the electrolyte/carbon black interface to give the optimisation algorithm the best chance to find optimal parameters for such case. Figure 4 first shows the comparison of the EIS curves between the Full model and the fitted model without the double layer model at the electrolyte/carbon black interface (denoted as Fitted model without CB_{DL}). It can be clearly seen that the Fitted model without CB_{DL} can still replicate the EIS curves relatively well in at least two cases (Figs. 4a and 4b), whereas in the Fig. 4c it was not able to properly capture the EIS curve. The good agreement in Figs. 4a and 4b is due to the fact that the optimisation algorithm adjusted parameters of the other double layer models, especially the double layer capacity at the Li-anode interface C_{eLi}^{DL}, in order to compensate for the missing electrolyte/carbon black double layer model. As a result, the fitted value for the double layer capacity at the Li-anode interface is $C_{eLi}^{DL} = 5.87$ F/m^2, which is an unreasonably high value, while this value in the Full model is $C_{es}^{DL} = 0.0134$ F/m^2.

Despite this fact, the EIS curve of the Fitted model without CB_{DL} shows a decrease in impedance, as can be seen in the Fig. 4c. The reason for this phenomenom might be related to the lower solid-phase diffusion constant at the higher lithiation level of the NMC at 3.665 V, which hinders the transport and increases the impedance. In the full model, the presence of the double layer model at the electrolyte/carbon black interface reduces this impedance at the cathode side, which is consistent with physicochemical processes in the cathode. Unlike, despite significantly and unreasonably increasing capacitance C_{eLi}^{DL} in the Fitted model without CB_{DL} model features worse agreement with the experimental data. Increasing capacitance C_{eLi}^{DL} indeed makes possible large accumulation of the charged species with are characterised by a much lower reaction energy barrier, and thus overpotential, compared to the (de)intercalating out of and into the particle. However, this leads to a further reduction in impedance in the anode and not in the cathode and the parametrisation routine tries to compensate this by a higher values of exchange current density $i_{0,es}$ for the electrochemical reaction at the particle's surface ($i_{0,es}$=10.91 A/m^2 (Fig. 4a); 14.48 A/m^2 (Fig. 4b); 4.53 A/m^2 (Fig. 4c)). These values are approximately higher by a factor of 2 compared to the values from the Full model in Table A·I. Therefore, such non-physicochemically consistent compensation does not make possible high fidelity replication of the experimental data.

The last set of curves in Fig. 4 shows the EIS spectra using the parameters of the Full model, where the double layer model at the electrolyte/carbon black interface was switched off and the fitted carbon black capacitance (Table A·I) was added to the capacitance of the double layer at the Li-anode. This analysis was performed to isolate the effect of shifting cathode capacitances to the anode, while keeping all

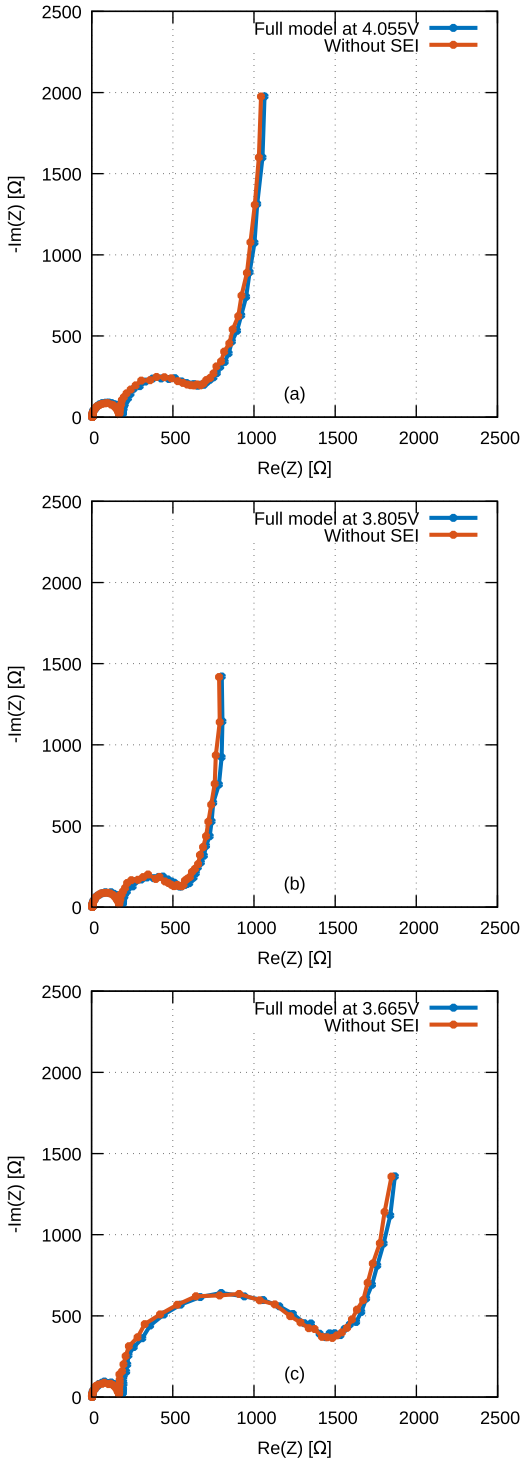

Figure 6. Comparison between the EIS results of the full model and the model without the discretised porous SEI layer. All other parameters were taken from the full model for all three cases from the Fig. 2.

other values of the model parameters. As expected, the resulting EIS spectra cannot replicate the high-frequency semicircle as well as elevated transition from the charge-transfer semicircle to the diffusion tail. This proves once again that it is necessary to include double layer model at the electrolyte/carbon black interface in order to increase physicochemical consistency of the model and, thus, its predictive capability while maintaining physically meaningful parameters, which is crucial for credible monitoring and diagnosis of batteries and avoids case-by-case fitting of the model for e.g. different cell formulations.

Diffusion impedance contribution of the porous SEI layer at the Li-anode interface.—To enhance physicochemical consistency of the model, a porous SEI layer was between the separator and metal Li-anode interface to model the additional contribution of the diffusion impedance of the Li-ions diffusing through the porous layer. The SEI forms at the surface of the metal Li-anode due to the redox potential of the anode which is outside the electrochemical stability window of the electrolyte.[71] For the porous SEI layer at the Li-anode interface the following assumptions were made following the reference:[72] the thickness of the layer was set to $L_{\mathrm{SEI}} = 20$ nm and does not change, and the porosity of the layer was set to value $\epsilon_{\mathrm{e}}^{\mathrm{SEI}} = 0.02$. The spatial numerical discretisation of the SEI layer was set to 4 control volumes. Figure 6 shows the comparison between the EIS curves obtained from the full model and parameters from Table A·I and the model where the discretised porous SEI layer was removed. There are only minor differences between the EIS curves for all three cases. This might be reasoned by the fact that the EIS measurements were performed on fresh cells with formation cycles (see Section Experimental on the electrode preparation and Section Electrochemical measurements on the electrochemical measurements in the appendix) and, therefore, only compact inorganic SEI was probably formed with a certain amount of the organic porous SEI. The optimisation algorithm calculated the optimal diffusion constant of Li-ions through the SEI to be $D_{\mathrm{e}}^{\mathrm{SEI}} = 1.573{\cdot}10^{-13}$ m^2/s. Therefore, the transport of Li-ions through the SEI layer is hindered compared to the typical diffusion constants of Li-ions in the electrolyte pores of the porous electrode. However, as can be seen from the sensitivity analysis in Fig. A·5, the notable impact on the EIS curves starts to appear with the values of diffusion constant $D_{\mathrm{e}}^{\mathrm{SEI}} = 4{\cdot}10^{-14}$ m^2/s and below. Therefore, the addition of a discretised model of the porous SEI layer is beneficial for a high degree of predictability of the model when analysing cells in different states of health, which in turn is important from a safety point of view.

Challenges related to the modelling of the inclination of the diffusion tail.—Modelling of the low frequency parts of the EIS spectrum, which are attributable to the slowest transport processes of Li in the electrode material has proven to be a challenging task. In many papers, this challenge has been by using the CPE elements, which lack a physical basis. In this section, therefore, the effects of introducing and varying physically meaningful parameters, i.e. the number and size distribution of the representative particles, on the diffusion part of the EIS spectra, in particular the inclination of the tail, are explained.

The widely adopted approach in the P2D models introduces a single representative particle of average size per each electrode control volume. To demonstrate the shortcomings of such an approach, an EIS simulation was performed with the single average sized representative particle ($R_{\mathrm{p}} = 3.23$ μm, denoted by "1 par" in Fig. 5). All other parameters were taken from the full model case. The results show that the single particle approach is not able to replicate the majority of the EIS spectra. In particular, it cannot replicate the tilt in the diffusion tail and instead exhibits a slope of almost 90 degrees, which corresponds to the capacitive behavior. To overcome these shortcomings, the model allows the addition of multiple differently sized particles into a single electrode's control volume. On the one hand, this is physically more consistent representation of the morphology of the electrode (see SEM image in Fig. A·1) but on the other hand, it also introduces different eigen time constants of the solid phase transport properties, which might be one of the possible reasons for the inclination of the diffusion tail at the low frequencies instead of relying on the CPE elements. Figure 5 also shows the variation of the number of representative particles in the control volume of the electrode with the remaining parameters taken from the full model cases with up to 9 differently sized particles. Even with the addition of only a few representative particles, the simulated EIS spectra are in better agreement with the

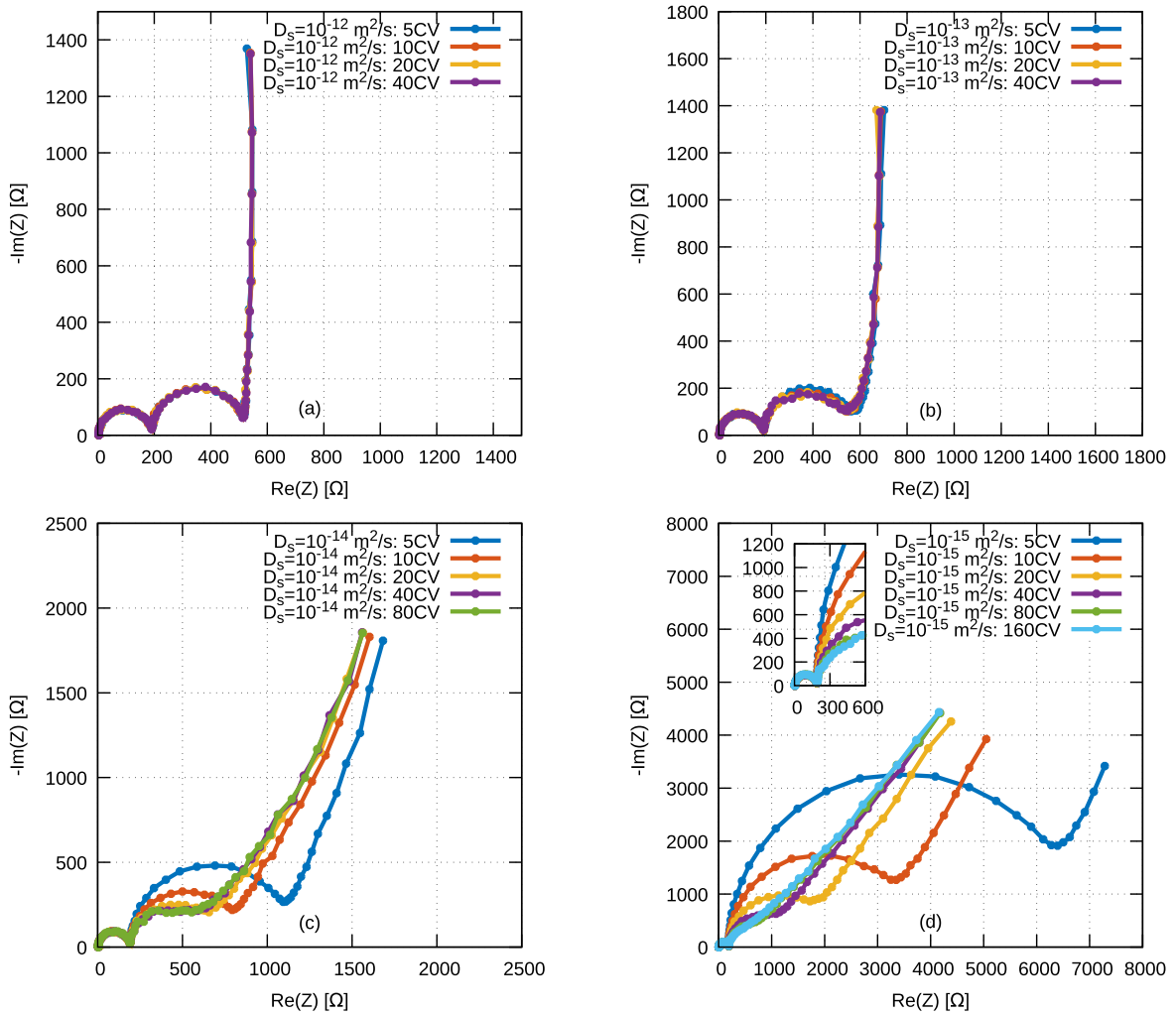

Figure 7. Numerical convergence of the EIS spectra over a range of four orders of the solid-phase diffusion constant when varying the discretisation number of the electrode particles: (a) $D_s = 10^{-12}$ m^2/s; (b) $D_s = 10^{-13}$ m^2/s; (c) $D_s = 10^{-14}$ m^2/s; and (d) $D_s = 10^{-15}$ m^2/s. With the exception of the diffusion constant, the parameters were taken from the full model case at 3.805 V (Fig. 2b). For the sake of clarity, the display range was not kept constant.

experimentally observed trend of the diffusion tail. The optimal number (12 particles) of representative particles was found by finding an optimal number of particles from pre-calculated list containing gaussian distributed particle sizes according to the manufacturer's size specifications of the NMC material in Table A·I. This result is presented as a "Full model" in Fig. 5 and previously compared with the experimental EIS curves in Fig. 2. This study demonstrates a physically based modelling approach, in this particular case, the inclusion of a number of size distributed representative particles, which significantly improves the agreement with the experimental data compared to models with a single representative particle of average size per electrode control volume.

Elucidating importance of proper numerical discretization to adequately model the EIS spectra.—Experimentally measured EIS spectra are often used for model based extraction of physically based parameters. In general, however, little attention is paid to the numerical convergence of the models used. In this section, we clearly show that discretisation significantly affects numerical convergence and can lead to completely unrepresentative physical parameters of the model, e.g. charge transfer current densities, double layer capacitances, etc.. The trade-off between numerical discretisation and numerical convergence is non-unique and strongly depends on the transport parameters in the governing equations.

Figure 7 shows the importance of sufficient particle discretisation when dealing with different orders of magnitude of solid phase diffusion constants that are relevant for the NMC cathode material across the SOC range. For clarification and demonstration purposes, we set the D_s to a constant value. In Fig. 7 the values of D_s range over four orders of magnitude from $D_s = 10^{-12}$ m^2/s to $D_s = 10^{-15}$ m^2/s.

For the first case with the highest diffusion constant $D_s = 10^{-12}$ m^2/s, five control volumes (CVs) are already sufficient to achieve the numerically convergent EIS spectrum (Fig. 7a) and ten CVs in the following Fig. 7b. By further decreasing the diffusion constant, more and more CVs are required to reach the convergent solution. This can be clearly seen in Figs. 7c and 7d, where the EIS spectra change significantly when the particle discretisation is increased and all other parameters are kept at the same values. More specifically, the oversized charge transfer semicircle starts to decrease its impedance value and more frequencies are being shifted from the charge transfer semi circle to the inclined diffusion tail. In Fig. 7d with the lowest diffusion constant $D_s = 10^{-15}$ m^2/s, the diffusion tail almost completely disappears at the lowest particle discretisation and then gradually starts to become more defined by increasing the discretisation. The inset in Fig. 7d shows the high frequency part of the EIS more in the detail and it can be seen that in this case 160 CVs may still not be a sufficient particle discretisation.

This observation is particularly important with regard to EIS fitting as an approach for determining parameters of the electrochemical system, e.g. a battery. Based on this observation, the optimisation of the model parameters to replicate the measured EIS curves (results presented in Fig. 2) was performed in this work with

the numerically convergent level of particle and electrode discretisation. It is also worth mentioning that a sufficiently high discretisation poses a challenge for real-time capable simulation modelling on embedded systems due to the high computational effort.

Conclusions

In this work, we, for the first time, present a numerical time-domain based electrochemical model capable of virtually replicating experimental EIS spectra with three superimposed high-frequency semicircles, an elevated transition to the diffusion tail, and a tilted diffusion tail at low-frequencies with high accuracy. This enhanced physicochemical consistency was achieved by significantly extending the state-of-the-art porous electrode models with innovative sub-models to simulate the double layer phenomenon associated with the carbon black/electrolyte interface, the double layer phenomenon at the metal-Li anode/electrolyte interface and the transport of charged species through the discretised porous SEI layer at the Li-anode interface. Furthermore, modelling of the inclination of the diffusion tail was made possible by introducing a number of representative active particles of different sizes into the electrode domain. In this way, it is possible to pinpoint a specific phenomenon within the cell, extract the corresponding physically meaningful parameters and determine and thus decipher their fingerprints in the EIS spectra. Furthermore, precise experimental measurements and a material characterization that enables the parameterisation of the electrochemical model were highlighted as an important component for achieving a good agreement with the experimental EIS.

Finally, we have provided detailed and consistent root-cause explanations for the need of a sufficiently high discretisation resolution of the particles when modelling in lithiation levels with expected low solid-phase diffusion constants, which have a significant impact on the results of the EIS spectra and consequently on the material properties extracted from the EIS spectra.

Due to an extended modelling framework with novel submodels, we were able to predict and decipher EIS spectra from the half-cell. The proposed electrochemical model with improved physico-chemical physicochemical consistency therefore enables for more consistent modelling of the EIS spectra at the full cell level and thus the extraction of important physical parameters of the battery from the EIS measurements. The modelling framework, therefore, allows the internal states of the battery to be determined by the non-invasive EIS measurements. The presented model can thus also be used also as a virtual sensor, which, among other applications, is of great importance for the next-generation battery management systems. The presented functions of the model open up perspectives for advanced monitoring, diagnostics and thus for battery management in order to prolong the longevity of the batteries and increase their safety.

Acknowledgments

The authors acknowledge support from the European Union's Horizon 2020 research and innovation programme under Grant Agreement No. 101103898 (NextBMS), 101137975 (InnoBMS), 101069743 (ADVAGEN), 101069686 (PULSELiON) and 101069910 (NEXTCELL). The authors also acknowledge financial support from the Slovenian Research Agency (research core funding No. P2-0401 and P2-0423 and projects J2-2494, J2-4463). The authors also acknowledge partial support from the Republic of Slovenia, Ministry of Higher Education, Science and Innovation, and from the European UnionNextGeneration EU in the framework of the project HyBReED, that is part of the Slovenian Recovery and Resilience Plan. The authors would also like to acknowledge the support of the HPC RIVR* consortium (www.hpc-rivr.si) for using the MAISTER HPC system at the University of Maribor (www.um.si).

Appendix

Experimental.— *Electrode preparation.*—Lithium nickel manganese cobalt oxide (NMC) electrodes with the composition

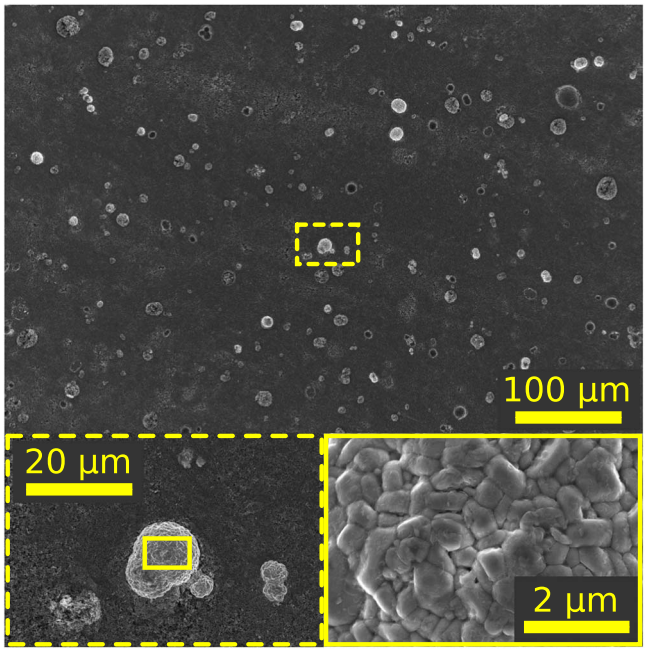

Figure A·1. SEM image of the top view on the diluted electrode with individual NMC agglomerates protruding from the sea of carbon black and binder. The magnification in the lower part of the Fig. shows the detailed morphology of the NMC agglomerate.

$LiNi_{0.82}Mn_{0.06}Co_{0.1202}$ were prepared by mixing the NMC material (MSE supplies, USA), carbon black (CB) and polyvinylene difluoride (PVDF, Sigma Aldrich) with N-Methyl-2-pyrrolidone (NMP, Merck) in a shaker mixer/mill (SPEX SamplePrep, USA) for 45 min. For simplicity in the text the NMC active material is abbreviated with the label NMC811. The electrodes for the GITT measurements were prepared with a (dry) composition corresponding to the mass ratio of NMC:CB:PVDF=90:5:5 and with carbon black Super C65T (Imerys). For the EIS measurements we prepared so-called "diluted electrodes" with particular dedicated mass ratio of NMC:CB:PVDF=20:75:5 exhibiting low fraction of NMC and a very high fraction of CB (Fig. A·1). The composition was selected with the purpose to ensure both: a) good electric (electronic) wiring between the aluminum current collector, along the CB "matrix" up to the individual isolated spherical secondary NMC particles and at the same time provide excellent ionic wiring (connectivity) between the bulk electrolyte in the separator and the surface of the individual secondary NMC particles. In order to avoid excessive side reaction(s) of electrolyte oxidation at the exposed CB surface we have in this case used low surface area Super C45 (Timcal).

The electrode slurry was coated on carbon coated aluminum foil (Armor, France) with a doctor blade, mounted on an automatic coater (MTI corporation). Obtained electrode film was in first step dried at 90 °C in a dynamic vacuum for at least 3 h. The final (dry) electrode loading of NMC active material was 5.2 mg/cm^2 for the electrodes that we used for GITT, and 55 μg/cm^2 for the "diluted electrodes" with reduced fraction of active material. From the obtained electrode sheet we cut out circular cathodes with a diameter of 16 mm (geometric area 2 cm^2) and pressed them in a hydraulic press with a force of 2.5 t (1.25 t/cm^2). The final thickness of electrodes for GITT measurements was 30 μm (calculated porosity ~40%). Obtained final thickness of diluted electrodes was about 8 μm (calculated porosity 84%–85%). Cathodes were in the second step additionally dried under dynamic vacuum at 110 °C over night (about 15 h) and transferred to an Argon-filled glove box (MBraun, Germany).

For anode we used a Li metal foil of thickness 110 μm that was cut into a circle (2.5 cm^2). The lithium surface was carefully scraped

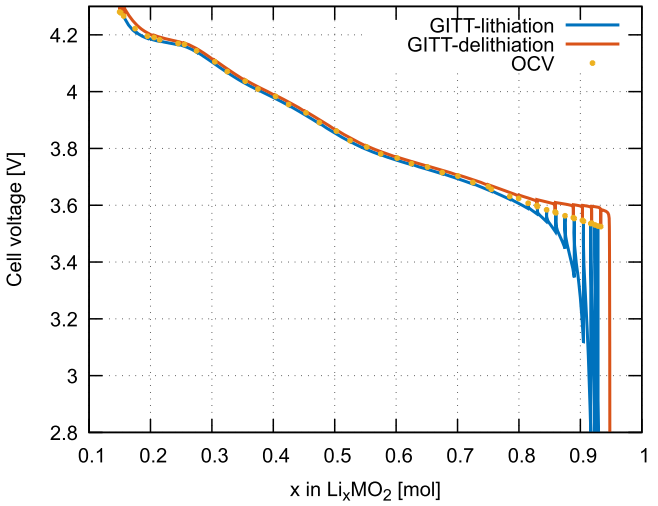

Figure A·2. GITT measurements in lithiation and delithiation direction and the corresponding OCV points determined from the end of each rest period as a function of Li content. Raw data available in the Supplementary information.

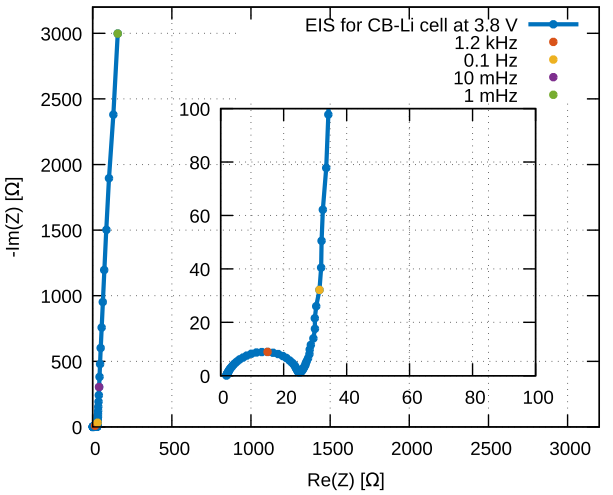

Figure A·3. Typical example of EIS Nyquist plot of measured impedance response of CB-Li cell exhibiting classic low-frequency capacitive impedance tail; in the case shown CB-based electrode was measured at 3.8 V (vs. Li^+/Li^0). Inset shows zoom-in part of the spectrum at high frequencies with a distinctive interfacial (SEI) impedance arc of lithium metal anode.

and rolled (inside an Ar-filled glove box) in order to expose fresh metal. In case of cells for the GITT measurements we prepared reference electrode (RE) from the same Li foil as it was used for the anode by first carefully rolling the foil to make it smooth and by cutting it in the shape of a triangle with a sharp tip.

Cell assembly.—Pouch type cells were assembled inside an Ar-filled glove box (water and oxygen content bellow 1 ppm) by properly stacking the electrodes and separator and sealing them into a triplex foil with pre-prepared 3 mm wide foil strips for contacts (Al for cathode, Cu for anode and RE in 3 electrode GITT cell). As separator we used glass microfiber filter paper GF/A (Whatman) of thickness 260 μm (manufacturer value, no pressure applied) and porosity 91% (calculated) that during assembly into the pouch cell squeezes to the final thickness of about 200 μm (calculated porosity 88%), separator geometric area was 3.8 cm^2. As electrolyte we used commercial 1 M $LiPF_6$ in EC/DEC=1:1 vol (LP40, E-lyte). For assembling of NMC-Li half cells we distributed electrolyte as follows: 15 μL for cathode, 15 μL for Li anode and 70 μL for separator. For assembling of NMC-Li 3 electrode cell we distributed electrolyte as follows: 15 μL for cathode, 15 μL for Li anode and 270 μL for 2 separators.

Electrochemical measurements.—The galvanostatic intermittent titration technique or GITT is a widely used technique for the electrochemical characterization of materials and electrodes used in batteries.[15] It uses a combination of short galvanostatic pulses followed by a long rest period. This sequence is repeated several times over the entire stoichiometry range of a single electrode (half cell) or over the entire state of charge (SoC) range for the full cells. Depending on the desired resolution of the results and the duration of the rest phases, the GITT experiments can take weeks to complete. Prior performing the GITT measurements we did 6 initial pre-cycles with CCCV charge and CC discharge between 2.8 V and 4.3 V (vs. Li RE) in order to go over "formation" processes and thus stabilize the cell response. After that we charged the cell with C/20 up to 4.3 V and performed GITT sequence with C/20 discharge pulses, followed by an appropriate relaxation periods. Figure A·2 shows such a measurement on the NMC811 half-cell. The first 3 pulses were equivalent to 2% of theoretical capacity, Q_{th}, and followed by corresponding relaxation times of 6 h. The next 2 pulses were equivalent to 3% of Q_{th} with 4 h of relaxation. The next nine pulses represented 5% of Q_{th} and the relaxation periods lasted for 4 h. As we approached lower states of charge (open circuit voltage, OCV, bellow 3.67 V), we again reduced duration of discharge steps with the aim to increase the number of measured states in this region and gradually increased the duration of the relaxation periods in order to really closely approach the true equilibrium condition. Specifically, we used 3 pulses representing 3% of Q_{th} with relaxation times of 6 h, 8 h and 12 h. Then we applied 6 pulses with 1.5% of Q_{th} with relaxation times of 12 h, 2 pulses with relaxation time of 16 h and finally 3 pulses with relaxation time of 20 h. The final 3 pulses in the lithiation direction were done with less than 1.5% of Qth (stopped by the lower cutoff voltage of 2.8 V) and with corresponding relaxation time of 24 h. After the last relaxation we discharged the cell with C/100 down to 2.8 V, and started with the charge GITT sequence. The first 4 pulses were equivalent to 1.5% of Q_{th} with a relaxation time gradually decreasing in the order: 20 h, 16 h, 14 h and 12 h. The next 3 pulses were equivalent to 3% of Q_{th} with relaxation time of 12 h, 10 h and 8 h. This was followed by 2 pulses equivalent to 3% of Q_{th} with 6 h of relaxation time. All subsequent charge pulses up to the upper cutoff voltage of 4.3 V represented 5% of Q_{th} and had a relaxation periods of 4 h. The GITT measurements was conducted at room temperature (24 °C) using the SP-200 potentiostat/galvanostat (Bio-Logic).

Figure A·2 additionally shows the OCV values, which are the most common output of the GITT measurements and are extracted from the voltage at the end of each rest period at a given stoichiometry level. These points are shown in Fig. A·2 with yellow dots. The stoichiometry range of the NMC material from $x = 0.157$ to $x = 0.933$ in the Fig. A·2 was determined from the Coulombic efficiency of the half-cell during the formation cycles. As a result of the accurate measurements with long rest periods toward the end of lithiation, there is no clear decrease in OCV values at high degrees of lithiation, as one might expect, but it decreases gradually (almost linearly), which is also consistent with the previously reported GITT experiments on the NMC material, e.g.[15] In addition, the OCV hysteresis between lithiation and delithiation points is also negligible.

In case of experiments that served for testing and verification of the time-domain based electrochemical model we first did initial pre-cycling of NMC-Li cell in order to go over the initial "formation" processes (e.g. the observed initial "activation" of the NMC material and formation of stable cathode-electrolyte interface). We performed 3 cycles with CCCV charge and CC discharge between 2.8 V and 4.3 V (vs. Li). For the first cycle, we used current density of C/15 followed by two C/10 cycles. After 3 h of relaxation we discharged

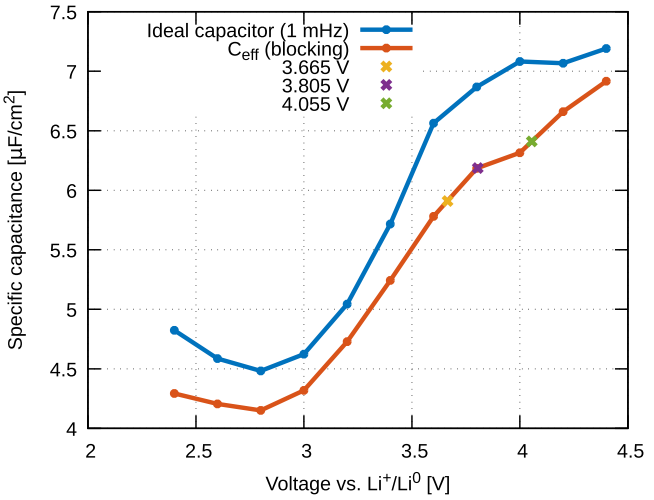

Figure A·4. Specific capacitance of electrical double-layer formed at the surface of CB particles (Super C65T, Imerys) immersed in 1 M $LiPF_6$ in EC/DEC=1:1 vol (LP40) electrolyte at 24 °C as a function of voltage. Capacitance was obtained by using the Brug type of relation (orange-coloured curve). The cross symbols show the values of the specific capacitance at three voltages at which the EIS measurements and model validation were carried out. For comparison, the values determined by applying a simple ideal capacitor approximation for measurement points at 1 mHz are shown (blue-coloured curve).

the cell down to 2.8 V using C/20 to ensure complete lithiation of the NMC material. After that we performed C/20 charging steps up to pre-defined voltages of 3.665 V, 3.805 V, and 4.055 V (vs. Li). At the each step we performed a voltage hold lasting for 6 hours. After voltage hold we measured the impedance response in each step by performing potential controlled EIS measurement in potentiostatic mode with 5 mV amplitude perturbation (3.5 mV rms) in the frequency range from 1 MHz down to 1 mHz (10 measured frequencies per decade). The measured galvanostatic curves and impedance spectra were obtained at room temperature (24 °C) using the WMP-300 potentiostat/galvanostat (Bio-Logic) with a built-in impedance module.

Experimental determination of specific double-layer capacitance due to carbon black conductive additive.—Specific double-layer capacitance due to carbon black conductive additive in the analysed cathodes was determined independently by additional experimental measurements. We performed systematic measurements of impedance responses of electrodes composed of only carbon black and binder. We prepared electrode composite mass containing 80 wt.% of carbon black (Super C65T, Imerys) and 20 wt.% of Teflon binder (PTFE 60 wt.% dispersion in H2O, Sigma-Aldrich) by mixing in presence of isopropanol in ball mill at low energy (30 mins at 300 rpm). The obtained composite was spread onto C-coated aluminum foilthe same type as used for preparation of the NMC cathodes. We cut out circular electrodes with diameter of 16 mm and pressed them (5 tonnes) to ensure good electronic connectivity and small contact resistance with current collector (aluminum foil). The obtained typical loading of carbon black was 6 mg per cm^2. After vacuum drying (90 °C over night) the electrodes were transferred into Ar-filled glove box and we prepared 2-electrode pouch-type cells with counter electrode made of lithium metal foil and by using glass microfiber filter paper GF/A (Whatman) separator; electrolyte was 1 M $LiPF_6$ in EC/DEC=1:1 vol (LP40, E-lyte).

At controlled temperature (in temperature chamber at 24 °C) we performed a series of EIS measurements at defined voltages. Prior an impedance measurement a cell was galvanostatically driven (100 μA) to a defined voltage, followed by a 4-hour voltage hold to ensure reaching equilibrium condition. We applied voltage sinusoidal perturbation (PEIS) with amplitude of 5 mV (3.5 mV

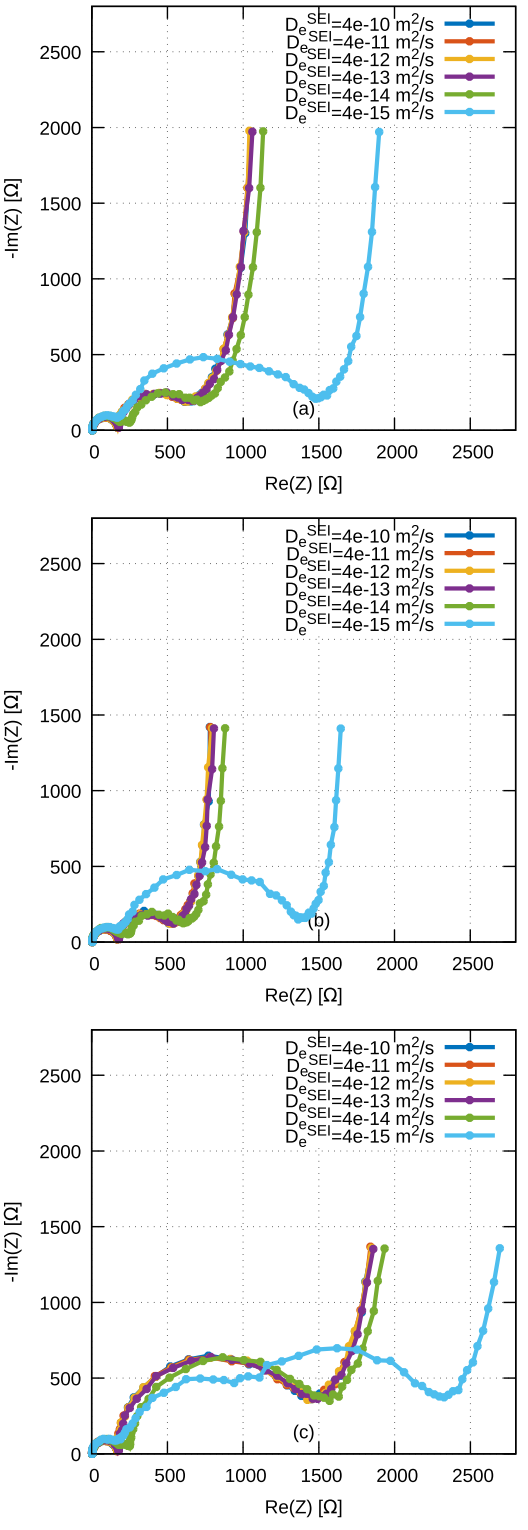

Figure A·5. Sensitivity analysis of impact of diffusivity of charged species through the discretised porous SEI layer on the EIS spectra for all three cases.

rms) in a frequency range from 1 MHz down to 1 mHz. Obtained EIS Nyquist spectra show (expected) capacitive behavior with a typical low-frequency capacitive impedance tail; an example of a typical EIS spectrum measured at 3.8 V (vs. Li^+/Li^0) is shown in Fig. A·3. Inset shows zoom-in part of the spectrum at high frequencies with distinctive interfacial (SEI) impedance arc of lithium metal anode (peak frequency at 1.2 kHz), followed by ion

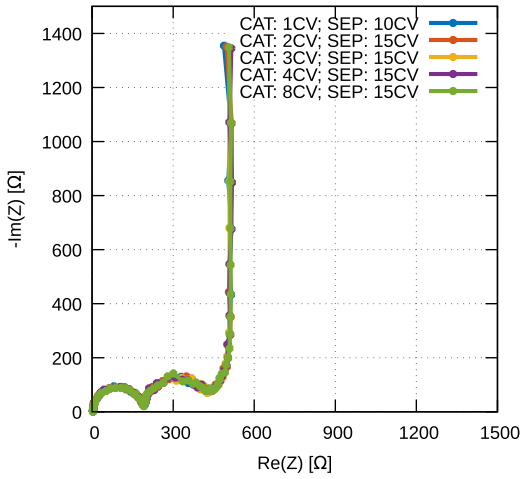

Figure A·6. Numerical convergence of EIS spectra when changing the discretisation number along the half-cell, i.e. the number of control volumes in cathode and separator. The parameters were taken from the full model case at 3.805 V (Fig. 2b), with exception of using a single particle per each control volume of the cathode.

migration resistance contribution of the carbon black electrode and diffusional resistance of electrolyte in separator, finally transitioning into vertical capacitive impedance tail at about 0.1 Hz.

The obtained EIS spectra were analysed by calculating effective capacitance of measured impedance tail by using the Brug type of relation for non-ideally polarised electrode.[73,74] For comparison we also did simple analysis where we applied relation for an ideal capacitor specifically for only the measurements at 1 mHz. Specific (area) capacitance was calculated by normalising the value of capacitance by the surface area of carbon black; the latter was calculated from the data about the mass and BET surface area of carbon black (62 $m^2\ g^{-1}$). The obtained results are shown in Fig. A·4 where it can be seen that simple ideal-capacitor approximation matches quite well with the results obtained by using the Brug relation, whereby the ideal-capacitor approximation overestimates capacitance values by about 5%–10%. It is interesting to note in Fig. A·4 that double-layer capacitance exhibits local minima at about 2.8 V (vs. Li^+/Li^0). At the voltages most relevant for the present study the corresponding values of specific capacitance are estimated to be: 5.9 $\mu F\ cm^{-2}$ (3.665 V), 6.2 $\mu F\ cm^{-2}$ (3.805 V), and 6.4 $\mu F\ cm^{-2}$ (4.055 V), respectively.

SEI diffusion impedance analysis.—To complement the Fig. 6 from the main text where the absence of the porous SEI layer at the Li-anode interface did not significantly change the EIS curves compared to the full model result, a sensitivity analysis was performed to analyze the impact of varying the value of the diffusion constant D_e^{SEI} of the Li-ions through the discretised SEI layer on the EIS spectra. This analysis is shown in Fig. A·5 and is applied to all three EIS curves that correspond to different levels of lithiation of the NMC811 material (Table I). The diffusion constant D_e^{SEI} was varied from $4 \cdot 10^{-10}$ m^2/s to $4 \cdot 10^{-15}$ m^2/s. By decreasing D_e^{SEI} one order of magnitude at time, until $D_e^{SEI} = 4{\cdot}10^{-13}$ m^2/s there is no major impact on the EIS curves in all three cases. With the $D_e^{SEI} = 4{\cdot}10^{-14}$ m^2/s a more pronounced increase in the real part of the impedance can be observed due to an additional diffusion impedance contribution. Further decreasing the D_e^{SEI} by another order of magnitude has an even more profound effect on the EIS curves. The real part of the impedance increases significantly, especially the middle frequency range in Figs. A·5a and A·5b, while the values of the complex part of the impedance remain the same. In addition, Fig. A·5c shows an emergence of the third semicircle, which is more clearly defined due to the increased SEI diffusion impedance.

Table A·I. Model parameters used in the full model simulations shown on Fig. 2. Remarks: †measured, ‡assumed from the literature, ⋆fitted, •calculated.

Parameter	Unit	Value
brugg	—	$1.5^{\ddagger}$[79]
$\epsilon_{e,cat}$	—	$0.845^{\bullet}$
$\epsilon_{e,sep}$	—	$0.880^{\bullet}$
ϵ_e^{SEI}	—	$0.02^{\ddagger}$[72]
D_e	m^2/s	$4 \cdot 10^{-10}$ ‡[80]
D_e^{SEI}	m^2/s	$1.573 \cdot 10^{-13}$ ⋆
κ_e	A/V m	$0.335^{\star}$
T	°C	$24.0^{\dagger}$
t_+	—	$0.363^{\ddagger}$[79]
a_{ecb}	1/m	$9.700 \cdot 10^{6\star}$
z_+	—	1
$\left(1 + \frac{\partial \ln f_{\pm}}{\partial \ln c_e}\right)(c_e, T)$	—	$1.0^{\ddagger}$[79]
σ	A/V m	$1.0^{\ddagger}$[81]
$\varphi^{V,b+cb}$	—	$0.141^{\bullet}$
$D_p = 2R_p$	μm	D10: ≈5 μm; D50: 9-15 μm; D90: <30 $\mu m^{\dagger}$;
	μm	$2R_{p,max}$: <45 μm; $2R_{p,mean} = 6.46 \mu m^{\dagger}$
$i_{0,es}$	A/m^2	$4.445^{\star}$ (Fig. 2a); $5.790^{\star}$ (Fig. 2b); $1.574^{\star}$ (Fig. 2c)
D_s	m^2/s	$4.723 \cdot 10^{-14\star}$ (Fig. 2a); $5.243 \cdot 10^{-14\star}$ (Fig. 2b); $2.186 \cdot 10^{-14\star}$ (Fig. 2c)
α_c	—	$0.5^{\ddagger}$[79]
α_a	—	$0.5^{\ddagger}$[79]
U^{OCV}	V	see Fig. A·2†
$i_{0,eLi}$	A/m^2	$0.766^{\star}$
U_{Li}^{OCV}	V	$0.0^{\ddagger}$[67]
C_{es}^{DL}	F/m^2	$0.831^{\star}$
C_{ecb}^{DL}	F/m^2	$0.0574^{\star}$
C_{eLi}^{DL}	F/m^2	$0.0134^{\star}$
L_{cat}	μm	$8.0^{\dagger}$
L_{sep}	μm	$200.0^{\dagger}$
L_{SEI}	nm	$20.0^{\ddagger}$[72]
$M_{am}/V_{M,am}$	kg/m^3	$4757.0^{\bullet}$

Numerical approach.—The set of coupled partial differential equations presented in Section Battery Model was numerically discretised in the two domains, i.e. the electrode domain and the particle domain, using the Finite Volume Method (FVM)[75] approach, resulting in a set of coupled Differential algebraic equations (DAE). DAE system was solved numerically with the Implicit Differential-Algebraic solver (IDA), a general purpose solver for the initial value problem (IVP) for systems of DAEs from the SUNDIALS software suite.[76,77] Numerical meshes of the computational domain consisting of cathode and separator were generated using the open source 3D finite element method (FEM) mesher Gmsh.[78] In this study, a 1D mesh was used, although the modelling framework also supports unstructured 2D meshes as shown in our previous work.[57] An in-house implemented library then computes all the necessary geometric and connectivity information needed for the FVM method. The particles, on the other hand, were discretised spherically in the 1D radial dimension. The numerical convergence related to the discretisaton of the particles has already been shown in the main text in Fig. 7. In addition to Fig. 7, where the importance of sufficient particle discretisation was highlighted, Fig. A·6 shows the convergence of the EIS spectra when changing the number of control volumes in the cathode and separator. To ensure comparable results between the different numerical meshes, a single particle of average size was selected for each control volume in the cathode domain. The SEI layer at the Li-anode was spatially discretised with 4 CVs in all cases. The Fig. A·6 shows that even the lowest discretisation

Table A·II. Sensitivity analysis of fitted parameters. Calculated RMSD value (Equation A·1) between the spectrum in which the individual parameter was perturbed by +10% and the non-perturbed spectrum obtained from the full model in units of Ω for all three EIS cases.

Parameter	RMSD [Ω] at 4.055 V	RMSD [Ω] at 3.805 V	RMSD [Ω] at 3.665 V
$i_{0,es}$	2.22885	1.92306	5.76618
$i_{0,eLi}$	1.51303	1.60592	1.68870
C_{es}^{DL}	0.42933	0.87595	1.19342
C_{eLi}^{DL}	0.66342	0.82745	1.21385
C_{ecb}^{DL}	0.99763	0.90381	2.42802
D_s	1.35406	1.11248	1.60231
D_e^{SEI}	0.58860	0.83526	1.23330
a_{ecb}	1.07893	0.95364	2.25624
κ_e	0.53386	0.93336	1.14559

mesh with 1 CV in the cathode and 10 CVs in the separator sufficiently models the EIS spectra. The reason for this result lies in the fact that the cathode in the half-cell itself is very thin and measures only 8 μm across and in combination with the high porosity of both the cathode and the separator favours the transport of Li-ions across the half-cell. Based on this result, the mesh with 15 control volumes was selected (1 CV in the cathode, 10 CVs in the separator and 4 CVs for the SEI layer) for the experimental validation with the Differential evolution algorithm.

Model parameters.—This Section presents model parameters (Table A·I) used in the modelling framework in the simulation results presented in this work.

Sensitivity analysis of the fitted parameters.—This Section contains an analysis of the fitted parameters for all three cases. The value of each individual fitted parameter (Table A·I) was relatively perturbed by +10%. The resulting EIS spectrum was compared with the unperturbed spectrum by calculating the RMSD in the units of Ω using the following equation

$$\mathrm{RMSD} = \frac{1}{N_{\mathrm{points}}}\sqrt{(\mathrm{Re}\,(\mathrm{Z})_{\mathrm{P}} - \mathrm{Re}(\mathrm{Z}))^2 + (\mathrm{Im}\,(\mathrm{Z})_{\mathrm{P}} - \mathrm{Im}(\mathrm{Z}))^2}\,, \qquad [\mathrm{A}\cdot 1]$$

where the letter P indicates the perturbed value of the real (Re(Z)) or complex part (Im(Z)) of the impedance Z in the EIS spectrum, which consists of N_{points} points. Table A·II shows the results of the sensitivity analysis. Both exchange current densities ($i_{0,es}$ and $i_{0,eLi}$), especially the $i_{0,es}$, exhibit higher sensitivity for all three EIS cases. This is to be expected as the impedance of the charge transfer is inversely proportional to the exchange current density.[46] Double-layer capacitances show a slightly lower sensitivity on average. The exception is the capacitance of the double layer at the carbon black interface at 3.665 V in combination with the specific surface area a_{ecb} of the carbon black that has also higher sensitivity in the latter case. The sensitivity of the solid phase diffusion constant D_s is on average lower than the exchange current density, for example, as it only affects the low-frequency parts of the EIS spectrum. Finally, the ionic conductivity κ_e and the diffusion constant of the Li-ions through the porous SEI layer D_e^{SEI} show a similar behavior and similar values of sensitivity, being lowest at 4.055 V in the first case and increasing with decreasing voltage.

ORCID

Igor Mele https://orcid.org/0000-0002-9071-7325

References

1. W. M. Dose, W. Li, I. Temprano, C. A. O'Keefe, B. L. Mehdi, M. F. L. De Volder, and C. P. Grey, "Onset potential for electrolyte oxidation and Ni-rich cathode degradation in lithium-ion batteries." *ACS Energy Lett.*, **7**, 3524 (2022).
2. Z. Ruff, C. Xu, and C. P. Grey, "Transition metal dissolution and degradation in NMC811-graphite electrochemical cells." *J. Electrochem. Soc.*, **168**, 60518 (2021).
3. A. Tornheim, S. Sharifi-Asl, J. C. Garcia, J. Bareño, H. Iddir, R. Shahbazian-Yassar, and Z. Zhang, "Effect of electrolyte composition on rock salt surface degradation in NMC cathodes during high-voltage potentiostatic holds." *Nano Energy*, **55**, 216 (2019).
4. Z. Zhang et al., "Cathode-electrolyte interphase in lithium batteries revealed by cryogenic electron microscopy." *Matter*, **4**, 302 (2021).
5. T. M. M. Heenan et al., "Identifying the origins of microstructural defects such as cracking within Ni-rich NMC811 cathode particles for lithium-ion batteries." *Adv. Energy Mater.*, **10**, 2002655 (2020).
6. Y. Mao et al., "High-voltage charging-induced strain, heterogeneity, and micro-cracks in secondary particles of a nickel-rich layered cathode material." *Adv. Funct. Mater.*, **29**, 1900247 (2019).
7. A. J. Merryweather, Q. Jacquet, S. P. Emge, C. Schnedermann, A. Rao, and C. P. Grey, "Operando monitoring of single-particle kinetic state-of-charge heterogeneities and cracking in high-rate Li-ion anodes." *Nat. Mater.*, **21**, 1306 (2022).
8. K. Marker, P. J. Reeves, C. Xu, K. J. Griffith, and C. P. Grey, "Evolution of structure and lithium dynamics in $LiNi_{0.8}Mn_{0.1}Co_{0.1}O_2$ (NMC811) cathodes during electrochemical cycling." *Chemistry of Materials*, **31**, 2545 (2019).
9. C. Xu, P. J. Reeves, Q. Jacquet, and C. P. Grey, "Phase behavior during electrochemical cycling of Ni-rich cathode materials for Li-ion batteries." *Adv. Energy Mater.*, **11**, 2003404 (2021).
10. E. Zsoldos, M. M. E. Cormier, N. Phattharasupakun, A. Liu, and J. R. Dahn, "How to measure solid state lithium-ion diffusion using the atlung method for intercalant diffusion." *J. Electrochem. Soc.*, **170**, 040511 (2023).
11. Battery2030 Initiative. https://battery2030.eu/research/roadmap/.
12. F. Ciucci, "Modeling electrochemical impedance spectroscopy." *Current Opinion in Electrochemistry*, **13**, 132 (2019).
13. N. Meddings et al., "Application of electrochemical impedance spectroscopy to commercial Li-ion cells: a review." *Journal of Power Sources*, **480**, 228742 (2020).
14. K. Zelič, T. Katrašnik, and M. Gaberšček, "Derivation of transmission line model from the Concentrated Solution Theory (CST) for porous electrodes." *J. Electrochem. Soc.*, **168**, 070543 (2021).
15. C. H. Chen, F. Brosa Planella, K. O'Regan, D. Gastol, W. D. Widanage, and E. Kendrick, "Development of experimental techniques for parameterization of multi-scale lithium-ion battery models." *J. Electrochem. Soc.*, **167**, 080534 (2020).
16. J. Moškon, J. Žuntar, S. Drvarič Talian, R. Dominko, and M. Gaberšček, "A powerful transmission line model for analysis of impedance of insertion battery cells: a case study on the NMC-Li system." *J. Electrochem. Soc.*, **167**, 140539 (2020).
17. B. Zhang, L. Wang, Y. Zhang, X. Wang, Y. Qiao, and S. G. Sun, "Reliable impedance analysis of li-ion battery half-cell by standardization on electrochemical impedance spectroscopy (eis)." *The Journal of Chemical Physics*, **158**, 054202 (2023).
18. M. Einhorn, F. V. Conte, C. Kral, and J. Fleig, "Comparison, selection, and parameterization of electrical battery models for automotive applications." *IEEE Transactions on Power Electronics*, **28**, 1429 (2012).
19. S. Skoog and S. David, "Parameterization of linear equivalent circuit models over wide temperature and SOC spans for automotive lithium-ion cells using electrochemical impedance spectroscopy." *Journal of Energy Storage*, **14**, 39 (2017).
20. J. Estaller, A. Kersten, M. Kuder, T. Thiringer, R. Eckerle, and T. Weyh, "Overview of battery impedance modeling including detailed state-of-the-art cylindrical 18 650 lithium-ion battery cell comparisons." *Energies*, **15**, 3822 (2022).
21. T. K. Dong, A. Kirchev, F. Mattera, J. Kowal, and Y. Bultel, "Dynamic modeling of Li-ion batteries using an equivalent electrical circuit." *J. Electrochem. Soc.*, **158**, A326 (2011).
22. T. Osaka, T. Momma, D. Mukoyama, and H. Nara, "Proposal of novel equivalent circuit for electrochemical impedance analysis of commercially available lithium ion battery." *Journal of Power Sources*, **205**, 483 (2012).
23. S. Barcellona, S. Colnago, L. Codecasa, and L. Piegari, "Unified model of lithium-ion battery and electrochemical storage system." *Journal of Energy Storage*, **73**, 109202 (2023).
24. F. T. Huld, Z. Yu, and F. Lou, "Unravelling the electrochemical impedance spectroscopy of silicon half cells with commercial loading." *Energy Advances*, **2**, 1176 (2023).
25. S. Cruz-Manzo and P. Greenwood, "Frequency transition from diffusion to capacitive response in the blocked-diffusion warburg impedance for eis analysis in modern batteries." *J. Electrochem. Soc.*, **167**, 140507 (2020).
26. T. Katrašnik, K. Zelič, A. Chowdhury, I. Pačnik, I. Mele, and A. Kravos, "Computer-implemented method and data processing system for modelling and/or simulating and/or emulating a battery." *United States Patent and Trademark Office*, United States of AmericaUS 11,480,616 B2 (2022).
27. S. Fletcher, "Tables of degenerate electrical networks for use in the equivalent-circuit analysis of electrochemical systems." *J. Electrochem. Soc.*, **141**, 1823 (1994).
28. X. Duan, F. Liu, E. Agar, and X. Jin, "Degradation diagnosis of $Li(Ni_{0.5}Mn_{0.2}Co_{0.3})O_2$/li half-cell by identifying physical parameter evolution profile using impedance spectra during cycling." *J. Electrochem. Soc.*, **170**, 040503 (2023).

29. A. Lasia, "The origin of the constant phase element." *J. Phys. Chem. Lett.*, **13**, 580 (2022).
30. I. Babaeiyazdi, A. Rezaei-Zare, and S. Shokrzadeh, "State of charge prediction of EV Li-ion batteries using EIS: a machine learning approach." *Energy*, **223**, 120116 (2021).
31. T. Pradyumna, K. Cho, M. Kim, and W. Choi, "Capacity estimation of lithium-ion batteries using convolutional neural network and impedance spectra." *Journal of Power Electronics*, **22**, 850 (2022).
32. Y. Liu, Q. Li, and K. Wang, "Revealing the degradation patterns of lithium-ion batteries from impedance spectroscopy using variational auto-encoders." *Energy Storage Materials*, **69**, 103394 (2024).
33. J. Newman and W. Tiedemann, "Porous-electrode theory with battery applications." *AIChE J.*, **21**, 25 (1975).
34. I. J. Ong and J. Newman, "Double-Layer Capacitance in a Dual Lithium Ion Insertion Cell." *J. Electrochem. Soc.*, **146**, 4360 (1999).
35. V. Boovaragavan, S. Harinipriya, and V. R. Subramanian, "Towards real-time (milliseconds) parameter estimation of lithium-ion batteries using reformulated physics-based models." *Journal of Power Sources*, **183**, 361 (2008).
36. A. M. Colclasure and R. J. Kee, "Thermodynamically consistent modeling of elementary electrochemistry in lithium-ion batteries." *Electrochimica Acta*, **55**, 8960 (2010).
37. N. Legrand, S. Raël, B. Knosp, M. Hinaje, P. Desprez, and F. Lapicque, "Including double-layer capacitance in lithium-ion battery mathematical models." *Journal of Power Sources*, **251**, 370 (2014).
38. T. R. Ashwin, Y. M. Chung, and J. Wang, "Capacity fade modelling of lithium-ion battery under cyclic loading conditions." *Journal of Power Sources*, **328**, 586 (2016).
39. S. Taslimi Taleghani, B. Marcos, and G. Lantagne, "Modeling and simulation of a commercial graphite-$LiFePO_4$ cell in a full range of C-rates." *Journal of Applied Electrochemistry*, **48**, 1389 (2018).
40. E. Hosseinzadeh, R. Genieser, D. Worwood, A. Barai, J. Marco, and P. Jennings, "A systematic approach for electrochemical-thermal modelling of a large format lithium-ion battery for electric vehicle application." *Journal of Power Sources*, **382**, 77 (2018).
41. A. Jokar, B. Rajabloo, M. Désilets, and M. Lacroix, "Review of simplified Pseudo-two-Dimensional models of lithium-ion batteries." *Journal of Power Sources*, **327**, 44 (2016).
42. J. Huang and J. Zhang, "Theory of impedance response of porous electrodes: simplifications, inhomogeneities, non-stationarities and applications." *J. Electrochem. Soc.*, **163**, A1983 (2016).
43. R. Scipioni, P. S. Jørgensen, C. Graves, J. Hjelm, and S. H. Jensen, "A physically-based equivalent circuit model for the impedance of a LiFePO4/graphite 26 650 cylindrical cell." *J. Electrochem. Soc.*, **164**, A2017 (2017).
44. Y. Li, M. Vilathgamuwa, T. Farrell, S. S. Choi, N. T. Tran, and J. Teague, "A physics-based distributed-parameter equivalent circuit model for lithium-ion batteries." *Electrochimica Acta*, **299**, 451 (2019).
45. E. Woillez and M. Chandesris, "Insight into LIB diffusion phenomena using analytical impedance models." *J. Electrochem. Soc.*, **170**, 070527 (2023).
46. J. P. Meyers, M. Doyle, R. M. Darling, and J. Newman, "The impedance response of a porous electrode composed of intercalation particles." *J. Electrochem. Soc.*, **147**, 2930 (2000).
47. N. A. Z. R-Smith et al., "Assessment of lithium ion battery ageing by combined impedance spectroscopy, functional microscopy and finite element modelling." *Journal of Power Sources*, **512**, 230459 (2021).
48. Y. Xie, J. Li, and C. Yuan, "Mathematical modeling of the electrochemical impedance spectroscopy in lithium ion battery cycling." *Electrochimica Acta*, **127**, 266 (2014).
49. M. Pathak, M. D. Murbach, C. Pathak, T. J. Jang, Y. Qi, D. T. Schwartz, and V. R. Subramanian, "Fast impedance simulation of lithium-ion batteries with pseudo-two dimensional electrochemical models." *J. Electrochem. Soc.*, **165**, A1324 (2018).
50. L. Teo, V. R. Subramanian, and D. T. Schwartz, "Dynamic electrochemical impedance spectroscopy of lithium-ion batteries: revealing underlying physics through efficient joint time-frequency modeling." *J. Electrochem. Soc.*, **168**, 10526 (2021).
51. M. D. Murbach and D. T. Schwartz, "Extending Newman's pseudo-two-dimensional lithium-ion battery impedance simulation approach to include the nonlinear harmonic response." *J. Electrochem. Soc.*, **164**, E3311 (2017).
52. L. Liu, J. Park, X. Lin, A. M. Sastry, and W. Lu, "A thermal-electrochemical model that gives spatial-dependent growth of solid electrolyte interphase in a Li-ion battery." *Journal of Power Sources*, **268**, 482 (2014).
53. L. Xue, X. Li, Y. Liao, L. Xing, M. Xu, and W. Li, "Effect of particle size on rate capability and cyclic stability of LiNi0.5Mn1.5O4 cathode for high-voltage lithium ion battery." *Journal of Solid State Electrochemistry*, **19**, 569 (2014).
54. R. Gopalakrishnan, Y. Li, J. Smekens, A. Barhoum, G. V. Assche, and N. Omar, "Electrochemical impedance spectroscopy characterization and parameterization of lithium nickel manganese cobalt oxide pouch cells: dependency analysis of temperature and state of charge." *Ionics*, **25**, 111 (2018).
55. I. Ezpeleta, L. Freire, C. Mateo-Mateo, X. R. Nóvoa, A. Pintos, and S. Valverde-Pérez, "Characterisation of commercial Li-ion batteries using electrochemical impedance spectroscopy." *ChemistrySelect*, **7**, e202104464 (2022).
56. I. Mele, I. Pačnik, K. Zelič, J. Moškon, and T. Katrašnik, "Advanced porous electrode modelling framework based on more consistent virtual representation of the electrode topology." *J. Electrochem. Soc.*, **167**, 060531 (2020).
57. T. Katrašnik, I. Mele, and K. Zelič, "Multi-scale modelling of Lithium-ion batteries: From transport phenomena to the outbreak of thermal runaway." *Energy Conversion and Management*, **236**, 114036 (2021).
58. T. Katrašnik, J. Moškon, K. Zelič, I. Mele, F. Ruiz-Zepeda, and M. Gaberšček, "Entering voltage hysteresis in phase-separating materials: revealing the electrochemical signature of the intraparticle phase-separated state." *Adv. Mater.*, **35**, 2210937 (2023).
59. K. Zelič and T. Katrašnik, "Computationally efficient quasi-3D model of a secondary electrode particle for enhanced prediction capability of the porous electrode model." *J. Electrochem. Soc.*, **169**, 040522 (2022).
60. D. A. G. Bruggeman, "Berechnung verschiedener physikalischer Konstanten von heterogenen Substanzen. I. Dielektrizitätskonstanten und Leitfähigkeiten der Mischkörper aus isotropen Substanzen." *Ann. Phys. (Berlin)*, **416**, 665 (1935).
61. M. Doyle, J. Newman, A. S. Gozdz, C. N. Schmutz, and J. M. Tarascon, "Comparison of modeling predictions with experimental data from plastic lithium ion cells." *J. Electrochem. Soc.*, **143**, 1890 (1996).
62. G. B. Less, J. H. Seo, S. Han, A. M. Sastry, J. Zausch, A. Latz, S. Schmidt, C. Wieser, D. Kehrwald, and S. Fell, "Micro-scale modeling of li-ion batteries: parameterization and validation." *J. Electrochem. Soc.*, **159**, A697 (2012).
63. S. Kosch, Y. Zhao, J. Sturm, J. Schuster, G. Mulder, E. Ayerbe, and A. Jossen, "A computationally efficient multi-scale model for lithium-ion cells." *J. Electrochem. Soc.*, **165**, A2374 (2018).
64. Z. Mao, M. Farkhondeh, M. Pritzker, M. Fowler, and Z. Chen, "Multi-particle model for a commercial blended lithium-ion electrode." *J. Electrochem. Soc.*, **163**, A458 (2016).
65. L. Cai and R. E. White, "Mathematical modeling of a lithium ion battery with thermal effects in COMSOL Inc. Multiphysics (MP) software." *Journal of Power Sources*, **196**, 5985 (2011).
66. M. Farkhondeh, M. Pritzker, M. Fowler, and C. Delacourt, "Mesoscopic modeling of a lifepo4 electrode: experimental validation under continuous and intermittent operating conditions." *J. Electrochem. Soc.*, **164**, E3040 (2017).
67. D. Ren, K. Smith, D. Guo, X. Han, X. Feng, L. Lu, M. Ouyang, and J. Li, "Investigation of lithium plating-stripping process in li-ion batteries at low temperature using an electrochemical model." *J. Electrochem. Soc.*, **165**, A2167 (2018).
68. R. Storn and K. Price, "Differential evolution-a simple and efficient heuristic for global optimization over continuous spaces." *Journal of Global Optimization*, **11**, 341 (1997).
69. K. Dokko, M. Mohamedi, M. Umeda, and I. Uchida, "Kinetic study of li-ion extraction and insertion at LiMn2O4 single particle electrodes using potential step and impedance methods." *J. Electrochem. Soc.*, **150**, A425 (2003).
70. S. Wu, B. Yu, Z. Wu, S. Fang, B. Shi, and J. Yang, "Effect of particle size distribution on the electrochemical performance of micro-sized silicon-based negative materials." *RSC Adv.*, **8**, 8544 (2018).
71. A. Wang, S. Kadam, H. Li, S. Shi, and Y. Qi, "Review on modeling of the anode solid electrolyte interphase (SEI) for lithium-ion batteries." *NPJ Computational materials*, **4**(1), 1–26 (2018).
72. S. Shi, P. Lu, Z. Liu, Y. Qi, L. G. Hector, H. Li, and S. J. Harris, "Direct calculation of Li-ion transport in the solid electrolyte interphase." *J. Am. Chem. Soc.*, **134**, 15476 (2012).
73. G. Brug, A. L. van den Eeden, M. Sluyters-Rehbach, and J. H. Sluyters, "The analysis of electrode impedances complicated by the presence of a constant phase element." *Journal of Electroanalytical Chemistry and Interfacial Electrochemistry*, **176**, 275 (1984).
74. B. Hirschorn, M. E. Orazem, B. Tribollet, V. Vivier, I. Frateur, and M. Musiani, "Determination of effective capacitance and film thickness from constant-phase-element parameters." *Electrochimica Acta*, **55**, 6218 (2010).
75. S. Mazumder, *Numerical Methods for Partial Differential Equations: Finite Difference and Finite Volume Methods* (Academic Press) (2015).
76. A. C. Hindmarsh, P. N. Brown, K. E. Grant, S. L. Lee, R. Serban, D. E. Shumaker, and C. S. Woodward, "SUNDIALS: Suite of nonlinear and differential/algebraic equation solvers." *ACM Transactions on Mathematical Software (TOMS)*, **31**, 363 (2005).
77. D. J. Gardner, D. R. Reynolds, C. S. Woodward, and C. J. Balos, "Enabling new flexibility in the SUNDIALS suite of nonlinear and differential/algebraic equation solvers." *ACM Transactions on Mathematical Software (TOMS)*, **48**, 1 (2022).
78. C. Geuzaine and J. F. Remacle, "Gmsh: A 3-D finite element mesh generator with built-in pre-and post-processing facilities." *International Journal for Numerical Methods in Engineering*, **79**, 1309 (2009).
79. B. Wu, V. Yufit, M. Marinescu, G. J. Offer, R. F. Martinez-Botas, and N. P. Brandon, "Coupled thermal-electrochemical modelling of uneven heat generation in lithium-ion battery packs." *Journal of Power Sources*, **243**, 544 (2013).
80. L. O. Valøen and J. N. Reimers, "Transport properties of lipf6-based li-ion battery electrolytes." *J. Electrochem. Soc.*, **152**, A882 (2005).
81. R. Tian, N. Alcala, S. J. O'Neill, D. V. Horvath, J. Coelho, A. J. Griffin, Y. Zhang, V. Nicolosi, C. O'Dwyer, and J. N. Coleman, "Quantifying the effect of electronic conductivity on the rate performance of nanocomposite battery electrodes." *ACS Appl. Energy Mater.*, **3**, 2966 (2020).